AD-A054 677 MISSION RESEARCH CORP SANTA BARBARA CALIF F/G 20/14
PROPAGATION OF MICROWAVE SATELLITE COMMUNICATION SIGNALS THROUG--ETC(U)
SEP 77 R W HENDRICK DNA001-76-C-0135
UNCLASSIFIED MRC-R-334 DNA-4412T NL

| OF |
AD
A054677

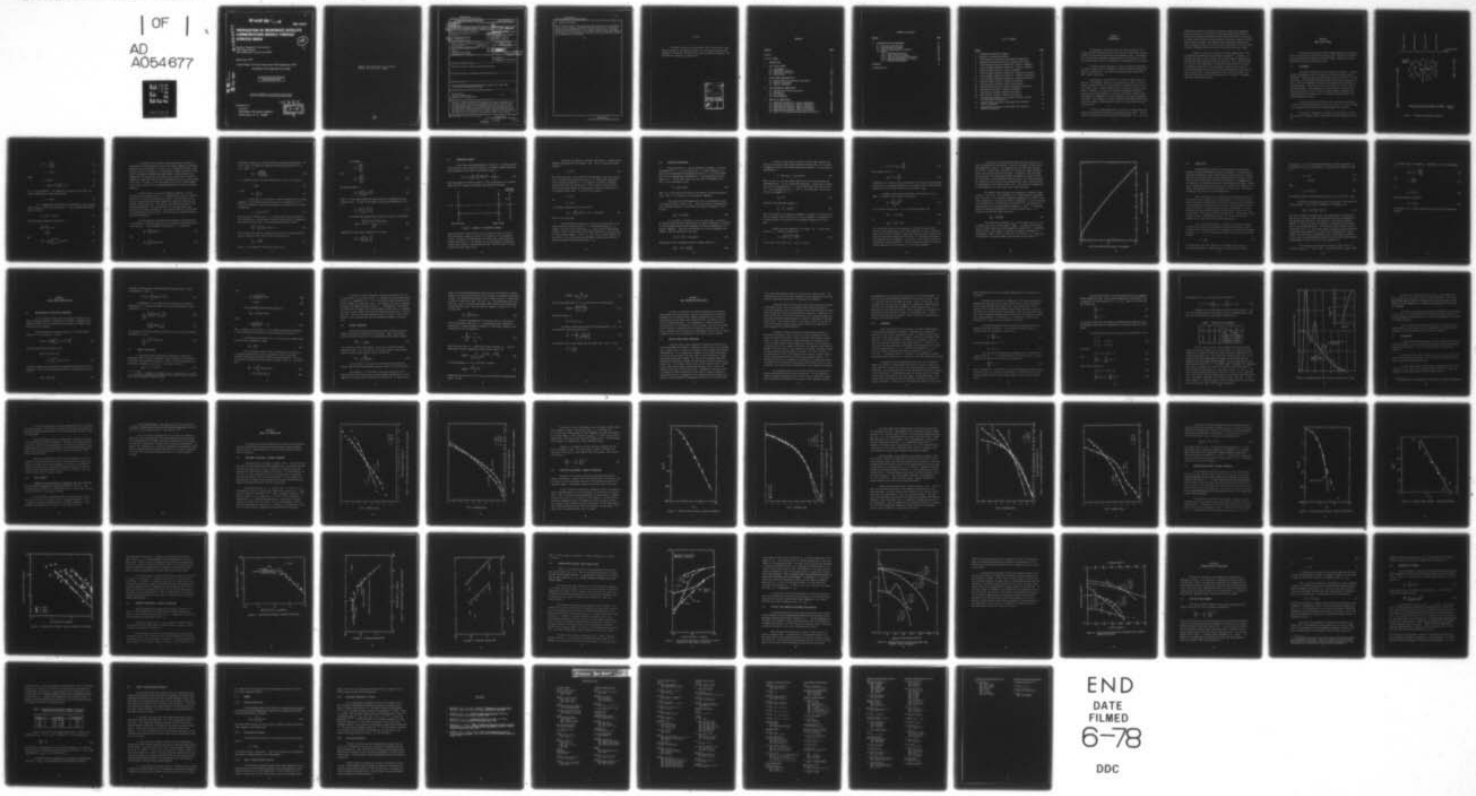

END
DATE
FILMED
6-78
DDC

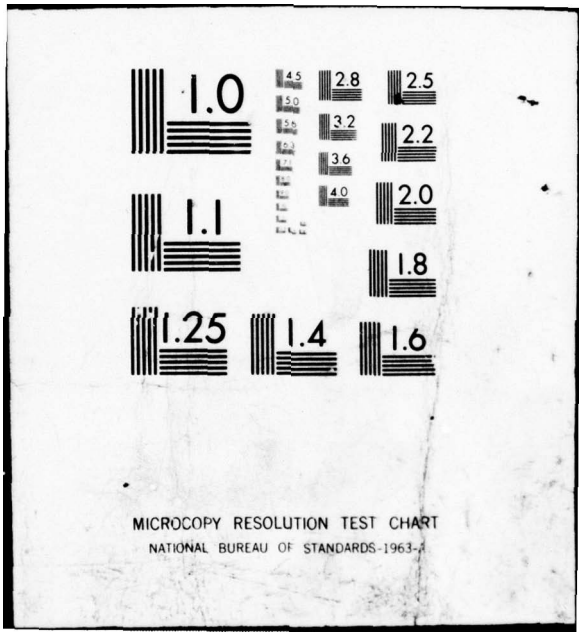
1.0
1.1
1.25
1.4
1.6
1.8
2.0
2.2
2.5
2.8
3.2
3.6
4.0
4.5
5.0
MICROCOPY RESOLUTION TEST CHART
NATIONAL BUREAU OF STANDARDS-1963-A

DNA 4412T

PROPAGATION OF MICROWAVE SATELLITE COMMUNICATION SIGNALS THROUGH STRIATED MEDIA

(12)

Mission Research Corporation
735 State Street
Santa Barbara, California 93101

September 1977

Topical Report for Period November 1975—September 1977

CONTRACT No. DNA 001-76-C-0135

APPROVED FOR PUBLIC RELEASE;
DISTRIBUTION UNLIMITED.

THIS WORK SPONSORED BY THE DEFENSE NUCLEAR AGENCY
UNDER RDT&E RMSS CODE B323076464 S99QAXHB05405 H2590D.

Prepared for
Director
DEFENSE NUCLEAR AGENCY
Washington, D. C. 20305

Destroy this report when it is no longer needed. Do not return to sender.

UNCLASSIFIED

SECURITY CLASSIFICATION OF THIS PAGE *(When Data Entered)*

REPORT DOCUMENTATION PAGE

READ INSTRUCTIONS BEFORE COMPLETING FORM

1. REPORT NUMBER: DNA 4412T	2. GOVT ACCESSION NO.
3. RECIPIENT'S CATALOG NUMBER	
4. TITLE (and Subtitle): PROPAGATION OF MICROWAVE SATELLITE COMMUNICATION SIGNALS THROUGH STRIATED MEDIA.	5. TYPE OF REPORT & PERIOD COVERED: Topical Report for period Nov 75—Sep 77
	6. PERFORMING ORG. REPORT NUMBER: MRC-R-334
7. AUTHOR(s): Roy W. Hendrick, Jr.	8. CONTRACT OR GRANT NUMBER(s): DNA 001-76-C-0135
9. PERFORMING ORGANIZATION NAME AND ADDRESS: Mission Research Corporation, 735 State Street, Santa Barbara, California 93101	10. PROGRAM ELEMENT, PROJECT, TASK AREA & WORK UNIT NUMBERS: NWED Subtask S99QAXHB054-05
11. CONTROLLING OFFICE NAME AND ADDRESS: Director, Defense Nuclear Agency, Washington, D.C. 20305	12. REPORT DATE: Sep 77
	13. NUMBER OF PAGES: 78
14. MONITORING AGENCY NAME & ADDRESS *(if different from Controlling Office)*	15. SECURITY CLASS *(of this report)*: UNCLASSIFIED
	15a. DECLASSIFICATION/DOWNGRADING SCHEDULE

16. DISTRIBUTION STATEMENT *(of this Report)*

Approved for public release; distribution unlimited.

17. DISTRIBUTION STATEMENT *(of the abstract entered in Block 20, if different from Report)*

18. SUPPLEMENTARY NOTES

This work sponsored by the Defense Nuclear Agency under RDT&E RMSS Code B323076464 S99QAXHB05405 H2590D.

19. KEY WORDS *(Continue on reverse side if necessary and identify by block number)*

Scintillation
Satellite Communication
Propagation in Striated Media

20. ABSTRACT *(Continue on reverse side if necessary and identify by block number)*

A series of multiple phase screen computations covered frequencies from 300 MHz to 8 GHz, rms electron concentration fluctuations from 10^4 to 10^7 electrons/cm^3 for layers 150 km and 500 km thick at mean ranges of 300 and 1000 km respectively. The integrated phase shift irregularities were characterized by both exponential and inverse cube power spectral density functions with various characteristic lengths. When fading (scintillation) was significant, the important, low amplitude portion of the receiver

DD FORM 1 JAN 73 1473 EDITION OF 1 NOV 65 IS OBSOLETE

UNCLASSIFIED

SECURITY CLASSIFICATION OF THIS PAGE *(When Data Entered)*

406 548

20. ABSTRACT (Continued)

signal is nearly Rician. The phase screen perturbations that are associated with structure of spatial wavelengths less than $\pi \ell_f$ (ℓ_f is the Fresnel distance) are those responsible for the multipath scintillations. The field strength decorrelation distance in the receiver plane is approximately $\sqrt{2}$ times the reciprocal of the rms transverse derivative of phase in the phase screens when scintillation is significant.

PREFACE

The author would like to thank Capt. Leon A. Wittwer, Air Force Weapons Laboratory, for making available to us his multiple phase screen propagation simulation; and Mark Frolli, Mission Research Corporation, who performed the computations reported here.

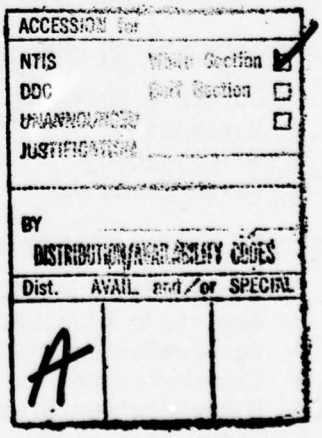

CONTENTS

CONTENTS (Continued)

LIST OF FIGURES

SECTION 1
INTRODUCTION

The detonation of nuclear devices at high altitudes (E- and F-layer altitudes) produces copious, persistent ionization which typically divides into striations aligned with the geomagnetic field. The propagation of radio waves through this medium results in perturbations of the wave front that may lead to a scintillating, fading signal at the receiver.

A previous report[1] developed an analytic treatment quantifying the signal characteristics if dimensions of the structure were small compared to a Fresnel zone. This work was extended to treat fading rates[2] under similar limitations.

Unfortunately, it appears that at satellite communication frequencies, the assumption that all of the structure is small is invalid. Analytic techniques have not been developed for structures about the size of a Fresnel zone. (Larger structures can be treated by ray optics techniques.) However, it is practical on modern, high-speed computers to represent the striated medium as a series of thin phase shifting screens and compute the propagation of waves through this by Fourier propagation techniques. This technique is called a Multiple Phase Screen (MPS) computation and produces a representative electric field distribution on the receiver plane.

A series of MPS computations[3] was run for an L-band signal traversing an environment described by an exponential power spectral density (PSD) of integrated electron concentration fluctuations. The results were

interpreted in terms of an effective variance of phase shift integrated along lines parallel to the line of sight to the satellite transmitter. The effective variance was defined as that which would lead to a prediction of similar signal characteristics when used with analytic expressions developed for small structure. The effective and actual phase variances were related through the fraction of the PSD that corresponded to structure with a spatial wavelength smaller than about three times the Fresnel length.

Methods of scaling the results of the MPS computations to other wavelengths and geometries were discussed in Reference 3. However, it appeared desirable to obtain results over a wider range of parameters and for different phase shift power spectral densities. This report describes the results of MPS computations at frequencies from 300 MHz to 8 GHz for two different phase PSD's, and at structural intensities such that the receiver plane statistics varied from trivial perturbations to fully developed scintillations. Primary emphasis was upon those environments for which the scintillations would be significant to a receiver. Altogether, about 2000 simulations were run.

SECTION 2
SMALL SCALE THEORY

This section will present relevant background about the effect of small scale structure extracted from previous work. There will be information concerning the description of the environment, dimensional scaling, amplitude scintillation, and fading rates.

2.1 ENVIRONMENT

The general configuration is that depicted in Figure 1. An undisturbed electromagnetic wave is incident on a region of varying index of refraction. The wave front is assumed planar, but the extension to a spherical shape is only mathematically more tedious rather than essentially different. The wave propagates through the structured medium followed by an unstructured one. The character of the wave front at a receiver plane is the desired output. The assumption of a plane wave and infinitely long striations parallel to the incident wave front renders the problem two-dimensional rather than three and is a reasonable representation of the nuclear degradation problem.

If the striations are inclined to the wave front, this analysis is valid so long as the inclination is not too close to $\pi/2$ and if proper care is taken of the increased path length through the striations.

The index of refraction of a plasma for microwaves (in regions where the wave frequency greatly exceeds the collision frequency) is given by

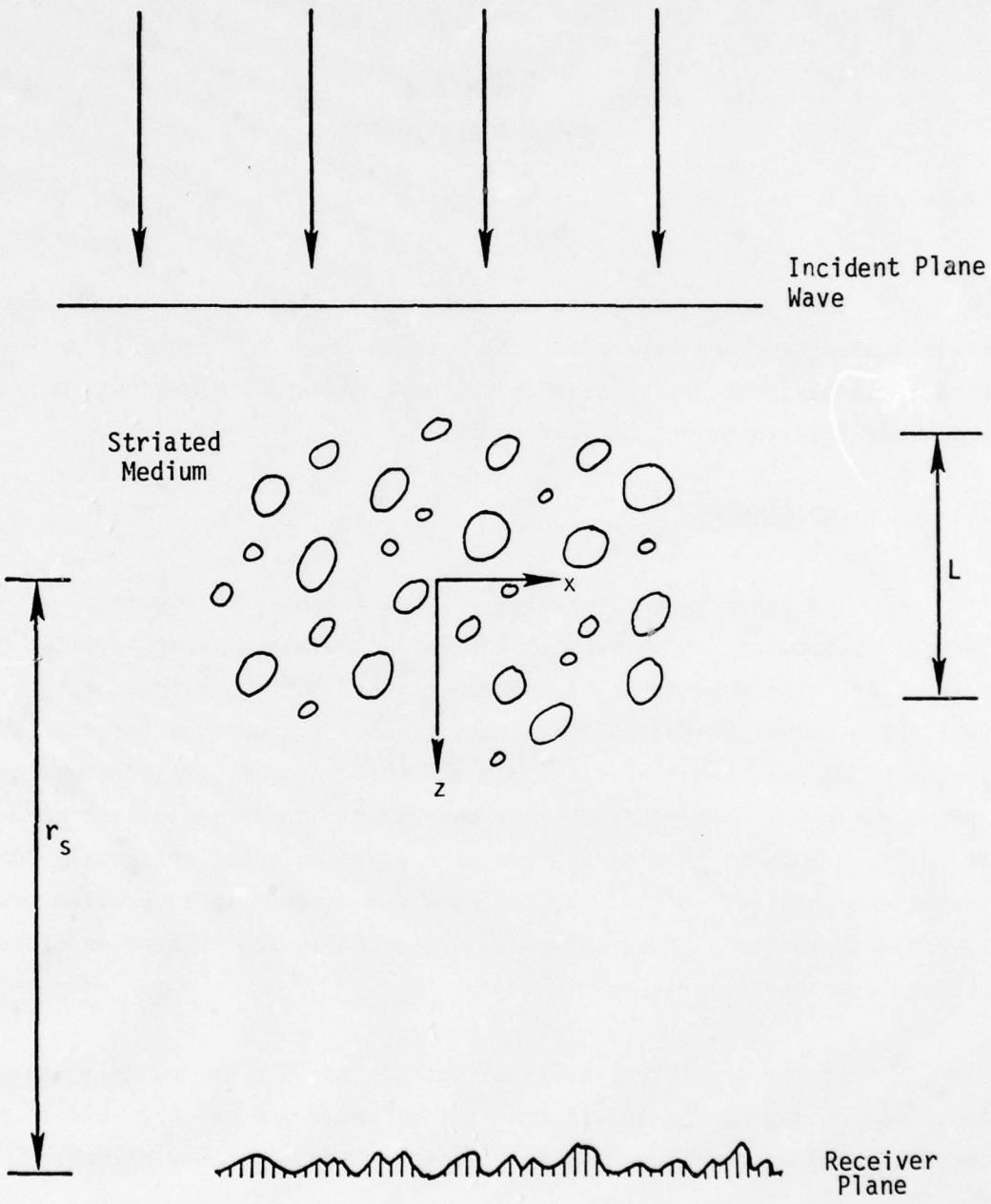

Figure 1. Propagation computation geometry.

$$\mu^2 = 1 - \frac{n_e e^2}{m\varepsilon_0 \omega^2} \tag{1}$$

$$= 1 - n_e/n_c \ , \tag{2}$$

where

$$n_c = \omega^2 m\varepsilon_0/e^2 \tag{3}$$

$$= 2.8278 \times 10^{11} \left(\frac{2\pi}{\lambda}\right)^2 \ \text{cm}^{-3} \ , \tag{4}$$

if λ is in centimeters. For conditions of concern to this study, the index of refraction is nearly unity so that

$$\mu = 1 - n_e/2n_c \ . \tag{5}$$

It is assumed that the medium can be described by a mean electron content $n_0(z)$, which varies slowly with z, and a fluctuating increment $n_e(x,z)$ such that

$$n_T = n_0(z) + n_e(x,z) \ . \tag{6}$$

The phase advance compared to the mean is

$$\frac{d\phi}{dz} = \frac{2\pi}{\lambda} (\mu_0 - \mu) \tag{7}$$

$$= \frac{\pi}{\lambda} \frac{n_e}{n_c} \ , \tag{8}$$

and

$$\phi(x) = \frac{\pi}{\lambda n_c} \int_{r_s - L/2}^{r_s + L/2} n_e(x,z)\, dz \tag{9}$$

For validity, the thin phase screen approximation requires the deflection of a wave traversing a screen to be small compared to structural dimensions of the striations. If this is true, propagation through a phase shifting screen at the middle of the medium with a phase shift $\phi(x)$ is equivalent to propagation through the actual medium. Multiple phase screen computations are applicable if the medium can be divided into a series of segments such that each can validly be considered thin, but the total medium is not thin. Of course, if the total medium is also thin, an MPS computation is still valid, but is an unneeded complication and requires needless computing.

The phase shift, ϕ, can be any arbitrary function. For the scattering case considered here, it is a random function and it is possible that only its statistical description is known. For this problem, ϕ is taken to be gaussianly distributed because the sight path intersects many randomly located striations. The central limit theorem then leads to the gaussian distribution. The characteristics of the phase screens are described by the phase variance, σ_ϕ^2 , and either the PSD or its equivalent, the autocorrelation function $R_\phi(\xi)$. The PSD and R_ϕ are related by being a Fourier transform pair.

For some purposes (one being the determination of fading rates), it is necessary to know the properties of the transverse spatial derivative of the phase ϕ'. In the appendices of Reference 3 it is shown that

$$\sigma_\phi^2 = \int_{-\infty}^{\infty} PSD_\phi(k)\ dk \tag{10}$$

and

$$\sigma_{\phi'}^2 = \int_{-\infty}^{\infty} k^2\, PSD_\phi(k)\ dk\ . \tag{11}$$

Equivalently, these may be obtained from the autocorrelation function. If we use $R_\phi(\xi)$ to denote the normalized autocorrelation function of ϕ (i.e., $R_\phi(0) = 1$),

$$\sigma_{\phi'}^2 = -\sigma_\phi^2 \left[\frac{d^2 R_\phi}{d\xi^2}\right]_{\xi=0} \quad . \tag{12}$$

ϕ' is important because the local deflection of a wave, θ, is given by

$$\theta = \frac{\lambda}{2\pi} \phi' \tag{13}$$

so that

$$\sigma_\theta^2 = \frac{\lambda^2}{4\pi^2} \sigma_{\phi'}^2 \quad . \tag{14}$$

At some point it is necessary to relate the phase shift to plasma parameters. One way that this has been done (as in Reference 1) is to visualize the medium as containing axisymmetric striations with an electron concentration:

$$n_e = n_0 \exp(-r^2/2a^2) \tag{15}$$

where n_0 may be a function of a, r is the distance from the striation axis, and there is a distribution of striation sizes given by a probability distribution function, $P(a)$. The following notation will be used:

$$\overline{n_0^k a^j} = \int_0^\infty n_0^k(a)\, a^j\, P(a)\, da \quad . \tag{16}$$

For the normal case that the striations overlap little, these expressions lead to a variance of the local electron concentration of

$$\sigma_n^2 = \pi m \overline{n_0^2 a^2} \tag{17}$$

where m is the number of striations per unit area.

If we define

$$a_e = \frac{\overline{n_0^2 a^2}}{\overline{n_0^2 a}} \tag{18}$$

and

$$a_f^2 = \frac{\overline{n_0^2 a^3}}{\overline{n_0^2 a}} \quad , \tag{19}$$

the phase variance is

$$\sigma_\phi^2 = \frac{2\pi^{7/2} mL}{\lambda^2 n_c^2 \sin\alpha} \overline{n_0^2 a^3} \quad . \tag{20}$$

where α *is the angle between the mean direction of propagation and the* striation axes. In terms of the variance of electron concentration, this is

$$\sigma_\phi^2 = \frac{2\pi^{5/2} L}{\lambda^2 \sin\alpha} \frac{a_f^2}{a_e} \frac{\sigma_n^2}{n_c^2} \quad . \tag{21}$$

The normalized autocorrelation function is given by the integral

$$R_\phi(\xi) = \frac{\int_{-\infty}^{\infty} n_0^2 a^3 \exp(-\xi^2/4a^2)\, P(a)\, da}{\overline{n_0^2 a^3}} \quad . \tag{22}$$

Expression 22 can be used in Equation 12 to yield:

$$\sigma_{\phi'}^2 = \frac{\pi^{5/2} L}{\lambda^2 a_e \sin\alpha} \frac{\sigma_n^2}{n_c^2} \quad . \tag{23}$$

2.2 DIMENSIONAL SCALING

If the thin screen approximation is valid (i.e., transverse deflection of energy is small within the medium), the Fresnel integral that gives the distribution of the field at the receiver plane is

$$E(y) = \frac{i}{\lambda r} \int_{-\infty}^{\infty} \exp\left[-\frac{i\pi(x-y)^2}{\lambda r} + i\phi(x)\right] dx \qquad (24)$$

where the geometry is shown in Figure 2. Basic assumptions are an incident plane wave and a medium that produces only moderate scattering.

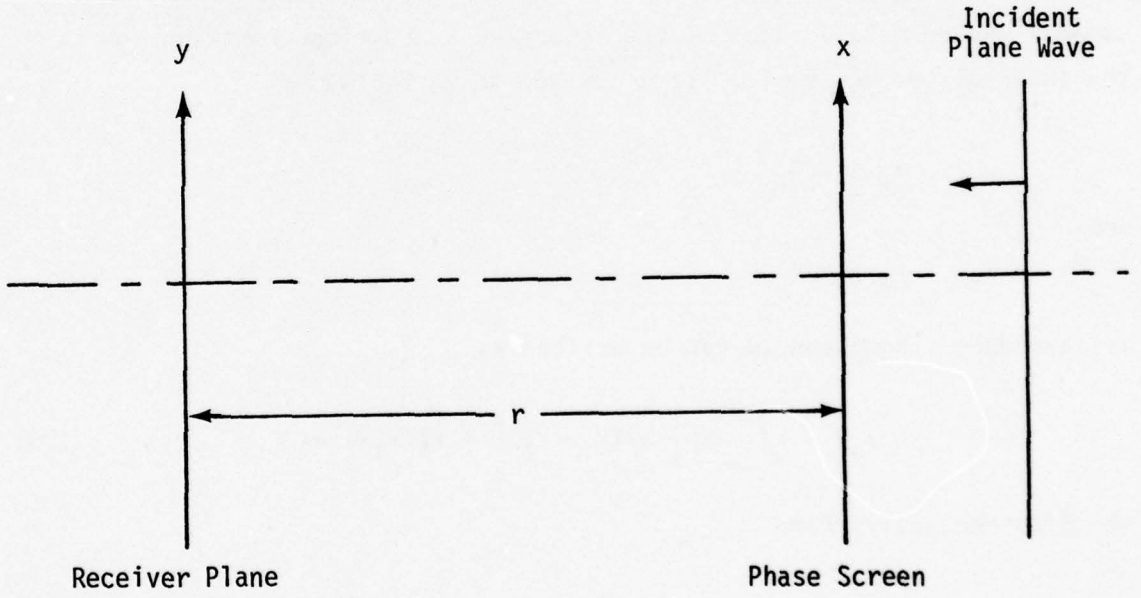

Figure 2. Geometry of propagation problem.

Obliquity factors of the order of $\cos\theta$ have been set equal to unity so that scattering at angles in excess of 0.1 radians or so is improperly treated. However, if scattering were that great, most systems would not operate satisfactorily. This geometry is also applicable to propagation between phase screens in the MPS approach where "receiver plane" is interpreted as the next phase screen.

Inspection of Equation 24 indicates that there is a characteristic dimension associated with the problem: $\sqrt{\lambda r}$. This is called the Fresnel distance:

$$\ell_f = \sqrt{\lambda r} \quad . \tag{25}$$

The Fresnel distance is that distance along the phase screen away from the direct, straight-line path which results in a π-radian phase retardation in the integral of Equation 24. It is basically a region of coherence. Outside that region, the phase factor $\pi x^2/\lambda r$ results in more and more closely spaced oscillations of the integrand so that the contribution to the integral becomes small. If a new set of variables

$$x_1 = x/\ell_f$$

and

$$y_1 = y/\ell_f$$

is introduced, Equation 24 can be written as

$$E(y_1) = i\int_{-\infty}^{\infty} \exp\left[-i\pi(x_1 - y_1)^2 + i\phi(x_1)\right] dx_1 \quad , \tag{26}$$

which is the scaled form.

The implication of Equation 26 is that if the phase shift at the scaled location in the phase screen x_1 is maintained constant as ℓ_f changes, the field at the scaled point y_1 in the receiver plane remains constant. Thus, if the structure of the phase variations is characterized by a decorrelation length ℓ and if σ_ϕ and ℓ/ℓ_f are held constant, the statistics in the receiver plane should remain constant except that the spatial correlation distance should vary as ℓ_f .

2.3 AMPLITUDE FLUCTUATIONS

The mean value of E can be obtained by averaging E over all distributions of ϕ. If the structure of ϕ is small compared to ℓ_f, this can be accomplished by multiplying the value of E as given by Equation 24 by the probability distribution of ϕ and integrating over the range of ϕ. For the small scale case, the order of integration over x and ϕ can be inverted to yield

$$\bar{E} = E_0 \exp(-\sigma_\phi^2/2) \tag{27}$$

where E_0 is the value of the field in the absence of any phase perturbations. This $\bar{E}$ is referred to as the specular component.

The output of the MPS computations will be interpreted in terms of an effective phase variance σ_{eff}^2. One of the means of estimating this will be through analysis of $\bar{E}/E_0$ where the inverse of Equation 27 will be used:

$$\sigma_{eff}^2 = 2\ \ell n(E_0/\bar{E}) \ . \tag{28}$$

It was argued in Reference 1, that the mean power is unaffected by scattering and that power removed from the specular component $(1 - \exp(-\sigma_\phi^2))$ is evenly divided between random components in phase and quadrature to the specular component. These are also referred to as real and imaginary components. Thus the variances of these are

$$\sigma_r^2 = \sigma_i^2 = E_0^2 [1 - \exp(-\sigma_\phi^2)]/2 \ . \tag{29}$$

Thus another way of estimating an effective phase variance is

$$\sigma_{eff}^2 = -\ell n[1 - 2\sigma_r^2/E_0^2] \ . \tag{30}$$

If there is some large scale phase structure that modulates the phase on the receiver plane without affecting the amplitude, it can lead to an apparent increase in the random quadrature component. Let the signal be represented by

$$S = [(\bar{E} + g_r\sigma_r) + ig_i\sigma_i] \exp(i\gamma) \tag{31}$$

where g_r and g_i are each random numbers from a unit variance gaussian distribution and γ is the random phase modulation. Based upon the assumption that the distribution of γ is sufficiently small that quartic terms in γ can be dropped and that σ_r and σ_i are equivalent, the variance of the real component of S is

$$\sigma_{S_r}^2 = \sigma_r^2 \tag{32}$$

and that of the imaginary component is

$$\sigma_{S_i}^2 = \sigma_i^2 + E_0^2 \overline{\sin^2\gamma} \quad . \tag{33}$$

Thus, the variance of the imaginary component is degraded by a phase modulation to a greater extent that that of the real component. Consequently, in the data analysis, the variance of the quadrature component will not be used.

Consider next the amplitude of the signal $|S|$. If the expression for S is taken from Equation 31,

$$|S| = \sqrt{(\bar{E} + g_r\sigma_r)^2 + g_i^2\sigma_i^2} \quad . \tag{34}$$

In the weak scintillation case, $\sigma_i << E_0$, so that

$$|S| \cong \bar{E} + g_r\sigma_r + \frac{g_i^2\sigma_i^2}{2\bar{E}} \quad . \tag{35}$$

The variance of $|S|$ is

$$\sigma_{|S|}^2 = \sigma_r^2 + \frac{1}{2}\frac{\sigma_i^4}{\bar{E}^2} \quad . \tag{36}$$

Consequently, for cases of weak scintillation, the variance of the magnitude of the field is a good approximation to the variance of the in-phase random component and can be used in Equation 30 to estimate σ_{eff}^2 .

A parameter often used for measuring scintillation is the S_4 index. Its square is the variance of the power

$$S_4^2 = \frac{\overline{|E|^4} - \overline{|E|^2}^2}{\overline{|E|^2}^2} \quad . \tag{37}$$

For the small structure case, E is Rayleigh-distributed, and

$$S_4^2 = 1 - \exp(-2\sigma_\phi^2) \ , \tag{38}$$

or

$$\sigma_{eff}^2 = -\frac{1}{2}\ln(1 - S_4^2) \ . \tag{39}$$

The problem with the use of this measure is that the S_4^2 index, which involves a mean fourth power of the signal amplitude, is quite sensitive to large values of field strength. Large scale focusing tends to produce more points of high field strength than would occur in a Rayleigh distribution, which distorts the data somewhat. In practice, values of S_4^2 in excess of 1 occurred for several simulations. This, of course, precludes the straightforward application of this measure to all the data generated.

A final means of establishing an effective phase variance is to count the probability of deep fades. This has the beauty of being exactly the phenomenon of concern. The probability of very deep fades (greater than 20 dB) is sufficiently small that the statistics on their occurrence are not very precise using the simulation. Fortunately, when deep fades become prevalent, the probability density distribution is nearly uniform, or at least has a constant gradient near the origin. For these conditions, the probability of an electric field amplitude less than a specified value is proportional to the square of that value. This allows the extrapolation of the probability of a rare event from a larger data base.

The specific means developed for establishing an effective phase variance is as follows. The probability of a 20-dB or greater fade (amplitude less than 0.1) is obtained by taking the probability of a fade to less than an amplitude of E_1/E_0 and dividing by $100(E_1/E_0)^2$. Data is available on the probability of a 20-dB fade as a function of β (the specular-to-random ratio) for a Rician distribution (Figure 3). Thus, β is obtained from the extrapolated probability of a 20-dB or greater fade. β is related to the effective phase variance by

$$\sigma_{eff}^2 = \ln\left(\frac{1+\beta}{\beta}\right) \quad . \tag{40}$$

The problem with estimating σ_{eff}^2 in this manner is that it can be applied only over a limited range of σ_{eff}^2. To obtain good estimates with the limited precision of fade probability requires that β be between about 0.5 and 5, which implies a variation in effective rms phase of 2. Consequently, because steps of a factor of 3 were used in σ_ϕ in most sets of simulations, few good estimates were obtained for each value of ℓ.

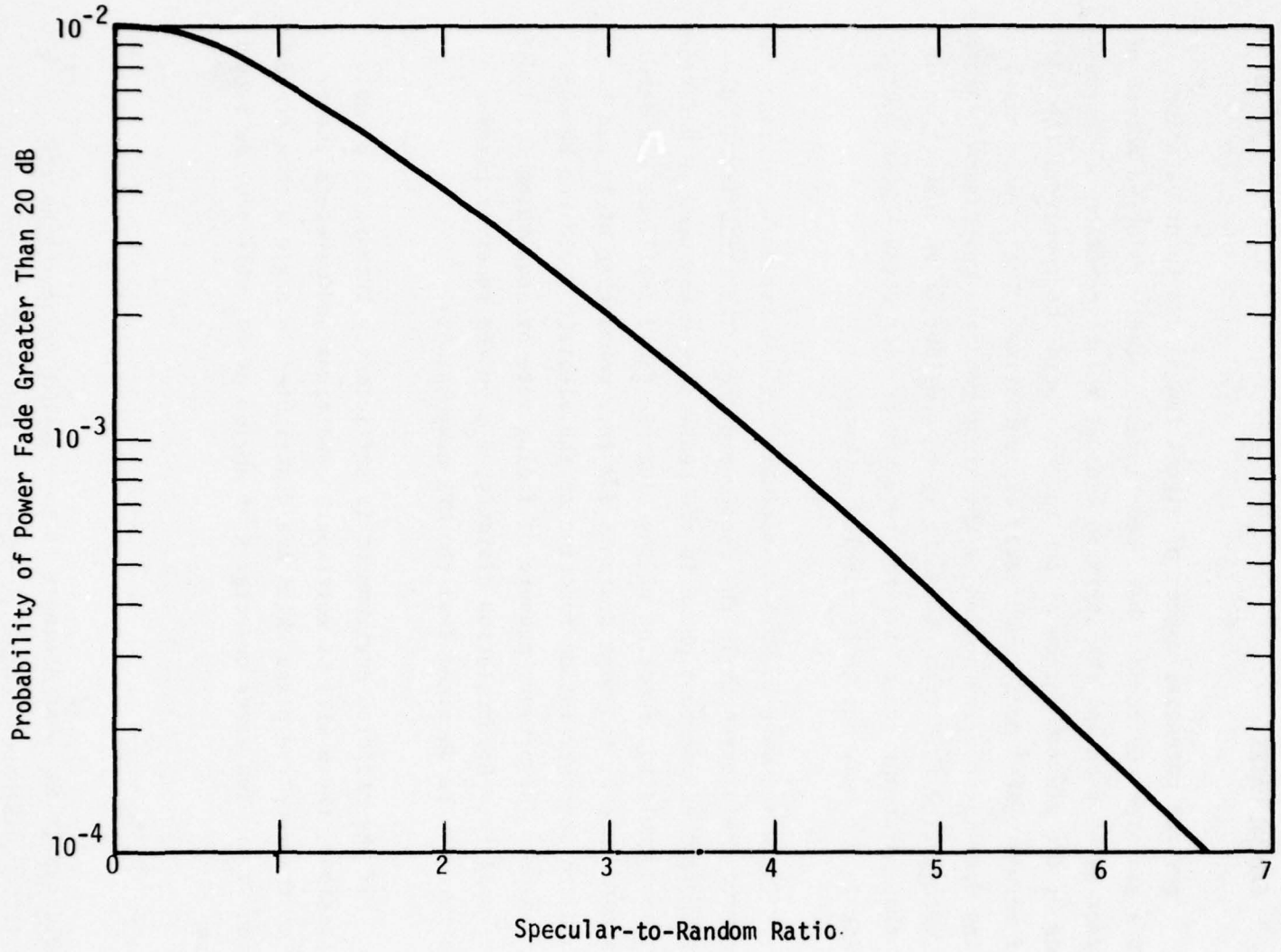

Figure 3. Fade probability variation with specular-to-random ratio.

2.4 FADING RATES

Several potential causes of signal fading due to propagation through a striated environment have been investigated: relative motion of the direct sight path and the striated plasma; relative motion of various portions of the plasma; motion of the source toward the receiver; the addition of more striated media; and decay of ionization. The primary cause of fading here is relative motion of the sight path and the plasma. Another way of visualizing this type of fading is to consider it as convection of a nearly time-invariant field past the receiver or vice versa. This source of fading is the only one to be considered here.

There are several ways to estimate the decorrelation distance of the electric field strength in the receiver plane. The variation in distance to points of constant phase in the phase screen was used in Reference 4; the autocorrelation function of the electric field amplitude was developed in Reference 2; the beat distance for rays converging at $\pm\sigma$ can be used; and the autocorrelation function of the electric field can be used in some cases. The primary measure of fading rate or, equivalently, fading distance will be a decorrelation distance, ℓ_c, on the receiver plane because this can be obtained from the MPS computations.

If the striated environment is sufficiently intense to produce scintillations, there will be multi-path conditions and wavelets interacting at the receiver plane which are distributed in angle with a standard deviation σ_θ. Two waves converging at angles of $\pm\sigma_\theta$ will provide a beat distance

$$\ell_b = \frac{\lambda}{2\sigma_\theta} \quad . \tag{41}$$

One would expect the beat distance to be somewhat greater than the decorrelation distance — larger perhaps by a factor of two or three.

The value of σ_θ can be obtained from Equation 14 and by noting that $\sigma_{\phi'}$ is related to σ_ϕ by a scale distance, s, obtained from Equations 21 and 23:

$$\sigma_{\phi'} = \sigma_\phi / s \tag{42}$$

$$= \sigma_\phi / \sqrt{2}\, a_f \quad . \tag{43}$$

Thus,

$$\ell_b = \sqrt{2}\, \pi\, a_f / \sigma_\phi \quad . \tag{44}$$

One therefore expects the decorrelation distance to be a few times a_f/σ_ϕ .

Consider the alternate derivation of the electric field autocorrelation function. This is given in Equation 77 of Reference 1 as:

$$R_E(\xi) = \exp\{-\sigma_\phi^2 [1 - R_\phi(\xi)]\} \quad . \tag{45}$$

Once the wave leaves the phase screen, the angular power spectral density and, hence, the electric field autocorrelation function are independent of the distance from the screen. The character of the field does change, however. At the screen the field amplitude is constant and the decorrelation is due to phase modulation. At sufficiently great distances and for sufficiently great σ_ϕ , wave mixing occurs, converting the phase modulation to amplitude scintillation with a statistically random phase or, equivalently, into statistically independent in-phase and quadrature components. In this limit, the autocorrelation function of each of the random components becomes equal to that of the initial field (Equation 45).

If one defines the decorrelation distance as that value of ξ for which $R_E(\ell_d) = e^{-1}$ and if $\sigma_\phi^2 >> 1$, only that portion of $R_\phi(\xi)$ where

it is nearly unity is significant. Consequently, it can be approximated by

$$R_E(\xi) \cong 1 - \frac{\sigma_{\phi'}^2 \xi^2}{2\sigma_\phi^2} \tag{46}$$

and

$$1 = \frac{\sigma_{\phi'}^2 \ell_d^2}{2} \tag{47}$$

or

$$\ell_d = \sqrt{2}/\sigma_{\phi'} \quad . \tag{48}$$

The use of Equation 45 leads to

$$\ell_d = 2\, a_f/\sigma_\phi \quad . \tag{49}$$

As expected, this is somewhat smaller than the previously computed beat distance.

SECTION 3
PHASE SCREEN CHARACTERISTICS

3.1 RELATIONSHIPS OF STATISTICAL DESCRIPTORS

In the literature dealing with scintillation produced by ionospheric striations there is a variability in notation. Although the conventions used here will not agree with those used by all workers in the field, they are as follows.

The normalized power spectral density of a zero mean random function y in an interval L will be

$$PSD_y(k) = \frac{1}{2\pi L}\left|\int_{-L/2}^{L/2} y(x)\, e^{ikx}\, dx\right|^2 \tag{50}$$

and the autocorrelation function will be

$$\begin{aligned} R_y^*(\xi) &= \left\langle y(x)\, y(x+\xi)\right\rangle \\ &= 1/L \int_{-L/2}^{L/2} y(x)\, y(x+\xi)\, dx \quad . \end{aligned} \tag{51}$$

As given, the power spectral density and autocorrelation function are not normalized. After the autocorrelation function is normalized to be one at $\xi = 0$,

$$R_y(\xi) = R_y^*(\xi)/\sigma_y^2 \quad . \tag{52}$$

The power spectral density and autocorrelation function form a Fourier transform pair. That is,

$$R_y^* (\xi) = \int_{-\infty}^{\infty} PSD_y(k)\, e^{-ik\xi}\, dk \quad . \tag{53}$$

In Reference 1 it was shown that the variance of the various derivatives of y could be obtained as the value of derivatives of $R_y(\xi)$ evaluated at $\xi = 0$:

$$\sigma^2_{\frac{d^n y}{dx^n}} = \left| \frac{d^{2n}}{d\xi^{2n}} \left(R_y(\xi) \right)_{\xi=0} \right| \sigma_y^2 \tag{54}$$

$$= \left| \frac{d^{2n}}{d\xi^{2n}} \left(R_y^*(\xi) \right)_{\xi=0} \right| \quad . \tag{55}$$

The derivative of the autocorrelation function can be obtained by operating on Equation 53. Thus,

$$\sigma^2_{\frac{d^n y}{dx^n}} = \int_{-\infty}^{\infty} k^{2n}\, PSD_y(k)\, dk \quad . \tag{56}$$

3.2 CHESNUT DISTRIBUTION

A plasma model often considered was inferred by Chesnut from photographic data of nuclear-detonation plasma striations. As pointed out by Chesnut, this model may be deficient in small scale structure which was obscured by photographic grain size. In any event, for this*:

$$R_\phi(\xi) = (1 + \xi^2/2\ell^2)^{-1} \tag{57}$$

*The ℓ used here is related to the a used above by $a = \ell/\sqrt{2}$. ℓ is used here to conform to the original Chesnut analysis and the multiple phase screen propagation program of AFWL.

and

$$\sigma_\phi^2 = \left(\frac{\sigma_n}{2n_c}\right)^2 \left(\frac{2\pi}{\lambda}\right)^2 2\sqrt{2}\, \ell\, L \tag{58}$$

$$= C\, 2\sqrt{2}\, \ell \ . \tag{59}$$

The corresponding power spectral density is

$$PSD_\phi = C\, 4\ell^2 \exp(-\sqrt{2}\, k\, \ell) \tag{60}$$

where

$$C = \left(\frac{\sigma_n}{2n_c}\right)^2 \left(\frac{2\pi}{\lambda}\right)^2 L \ , \text{ and} \tag{61}$$

PSD_ϕ is taken to be one-sided (i.e., the portion associated with negative k has been folded over and added to that associated with positive k).

The variances of derivatives of ϕ are most easily obtained from the power series expansion of $R_\phi(\xi)$

$$\sigma_{\phi'}^2 = \sigma_\phi^2/\ell^2 \ . \tag{62}$$

If only striations smaller than a particular size are effective at producing scintillation, one may reasonably ask what is the phase variance associated with structure smaller than some threshold. This can be obtained by integrating the PSD from the threshold value k_1 to infinity. Thus,

$$\sigma_\phi^{2*} = C\, 4\, \ell^2 \int_{k_1}^{\infty} \exp(-\sqrt{2}\, k\ell)\, dk \tag{63}$$

$$= 2\sqrt{2}\ C\, \ell \exp(-\sqrt{2}\, k_1\, \ell) \ . \tag{64}$$

On the basis of the dimensional scaling by the Fresnel size, if the concept of a k_1 cutoff is valid, k_1 should be inversely proportional to the ℓ_f. Consequently, for $\ell >> \ell_f$ the effective phase variance should decline rapidly with increasing ℓ/ℓ_f. This reflects the lack of structure at spatial wavelengths much smaller than ℓ. Measurements in the natural ionosphere have not shown such a rapid structural cutoff and it is currently felt by many that, indeed, film grain did obscure the fine detail in nuclear test data. The main reason for proceeding with this model is that it does present a rather extreme model that may reasonably represent a limiting case.

3.3 NATURAL IONOSPHERE

Electron concentration profiles have been obtained by probes on rockets and satellites traversing the ionosphere. Many of the spectra display the general character of a one-dimensional power spectral density

$$PSD^1_{n_e} \propto \frac{1}{1 + k^2\ell^2} \tag{65}$$

—an "inverse k square" relationship. This will be called the natural ionospheric model. The line integral of electron content or phase perturbation will have a power spectral density of the form

$$PSD_\phi = \frac{\sigma_\phi^2 \ell}{(1 + k^2\ell^2)^{3/2}} \quad . \tag{66}$$

For this model, it is easier to work with the power spectral density than with the autocorrelation function, which is a Bessel function.

The parameter ℓ in the PSD is called the outer scale size. There must also be an inner scale size which reduces the PSD_ϕ below that of Equation 66 in order that the variance of derivatives of ϕ remain finite.

There is no good experimental data giving an inner scale because it usually appears to be below the resolution (tens of meters) of experiments performed to date. For demonstration purposes, take an upper value of k beyond which the PSD is assumed to be zero. Call this k_m. The experimental data indicate that $k_m \ell >> 1$; the upper wave number cutoff affects the normalization of the PSD_ϕ very little. We can obtain by integrals of powers of k^2 and the PSD_ϕ that

$$\sigma_{\phi'}^2 = \frac{\sigma_\phi^2}{\ell^2} \ell n(2 k_m \ell) \quad . \tag{67}$$

A specific representation of striations which is convenient to work with and which yields the k^{-2} one-dimensional power spectrum is a distribution of gaussian profile striations in which their location is random and their size distribution is

$$P_s = \begin{cases} 0 & s < s_1 \\ a/s^2 & s_1 < s < s_2 \\ 0 & s > s_2 \end{cases} , \tag{68}$$

where the inner scale s_1 is much smaller than the outer, s_2. The one-dimensional electron concentration power spectral density is

$$PSD_n^1(k) = \frac{\sigma_n^2}{\sqrt{\pi}\,(s_2 - s_1)\,k^2} \left(e^{-k^2 s_1^2} - e^{-k^2 s_2^2} \right) . \tag{69}$$

At long wavelengths ($k << 1/s_2$), the PSD is constant

$$PSD_n^1(k) = \frac{\sigma_n^2 (s_2 + s_1)}{\sqrt{\pi}} \quad . \tag{70}$$

Between the two scales ($1/s_2 << k << 1/s_1$), the PSD exhibits an approximately inverse k^2 form

$$PSD_n^1(k) = \frac{\sigma_n^2}{\sqrt{\pi}\,(s_2 - s_1)\,k^2} \quad . \tag{71}$$

And at short wavelengths ($k >> 1/s_1$), the PSD cuts off exponentially

$$PSD_n^1(k) = \frac{\sigma_n^2 \exp(-k^2 s_1^2)}{\sqrt{\pi}\,(s_2 - s_1)\,k^2} \quad . \tag{72}$$

The phase variance is

$$\sigma_\phi^2 = C\sqrt{\pi}\,(s_1 + s_2) \quad . \tag{73}$$

The phase variance associated with structure having a $k > k_1$ can be obtained by integrating Equation 66.

$$\sigma_\phi^{2^*} = C\sqrt{\pi}\,\ell\left[1 - \frac{k_1\ell}{\sqrt{1 + k_1^2\ell^2}}\right] \tag{74}$$

If the outer scale is much larger than the cutoff size, $k_1\ell >> 1$, and

$$\sigma_\phi^{2^*} = \frac{C\sqrt{\pi}}{2\,\ell\,k_1^2} \quad . \tag{75}$$

SECTION 4
WAVE PROPAGATION COMPUTATIONS

In order to investigate the detailed character of the electric field produced by plasma having structure with characteristic dimensions comparable to the Fresnel length, computer simulations were run using a multiple phase screen (MPS) code[5] provided by Capt. Leon Wittwer of the Air Force Weapons Laboratory. For completeness, a short description of characteristics of the simulation will be included. This will be followed in this section by a description of our means for removing large scale phase variations usually referred to as detrending, criteria used in setting up phase screens, and a presentation of the matrix of cases computed.

4.1 MULTIPLE PHASE SCREEN SIMULATION

A multiple phase screen propagation simulation divides the disturbed environment into segments, collapses the phase shift in each segment onto a single plane or screen, and propagates a wave through this idealized representation. It is assumed that a segment of the striated environment can be chosen sufficiently thin that there is little deviation of energy propagating through that segment, and, hence, the integrated phase shift experienced traversing the segment can be treated as though occurring at a single plane. The electric field incident on the plane or screen is multiplied by the complex number representing the phase shift to obtain the electric field vector leaving the screen. Propagation to the next screen is computed by Fourier analyzing the field into its angular components, multiplying these by a propagation vector (different for each angular component), and transforming the propagated field back into its spatial form

at the next phase shifting screen or finally at the receiver plane. The simulation utilizes fast Fourier transforms and our computations used 2048 points in each phase screen and in the angular distributions.

There are several ways one might choose the distribution of phase on the phase screen. One is to randomly locate striations having the structural properties and size distribution desired and integrate the phase shift through this explicit representation of striations. Another way is to derive analytically a statistical description of the integrated phase and from this description generate directly a specific realization of the integrated phase. This latter procedure is the faster of the two and for the cases to be treated, produces phase screens statistically equivalent to those produced by the former procedure.

The phase screens generated have a phase whose amplitude is gaussianly distributed. This is valid if every ray through the screen intersects several striations so that the central limit theorem is applicable. To avoid the necessity of empty guard bands at the edge of the screen and large angular Fourier components associated with a difference in phase shift at the two edges of the screen (the angular Fourier analysis assumes the field is cyclic in the width of the screens), the phase screens are made continuous from one edge to the other. The basic statistic of the phase which is used is the autocorrelation function. However, this is Fourier transformed to obtain the spatial power spectral density. The amplitude of each Fourier component is multiplied by a random phase (which is different for each specific realization) and the phase screen is reconstructed by the inverse Fourier transformation of the randomized components.

The simulation usually was run twenty times for each particular problem using different phase screen realizations. The code generates various averaged descriptions of the electric field at the receiver plane. These include the distribution of the electric field components in-phase

and quadrature to the undisturbed field and the total field amplitude. It also gives the two-dimensional distribution of the electric vector. That is, it gives a table of the number of points $N(n,m)$ at which $\frac{n}{10} - 0.05 < E_r \leq \frac{n}{10} + 0.05$ and $\frac{m}{10} - 0.05 < E_i \leq \frac{m}{10} + 0.05$. Except for a normalizing factor, it is the two-dimensional probability density function of E. It is displayed as a plot with the value of $N(n,m)$ printed at a coordinate n,m. These plots will be referred to simply as "distribution of E." Various statistical descriptors are computed — such as the spatial autocorrelation function of the electric field.

4.2 DETRENDING

Often the character of scintillation in a radio signal channel, either measured through the ionosphere or computed with a simulation, is obscured by large, slowly varying phase shifts. In actual receiver equipment, this slowly varying phase is removed by AFC circuits and phase tracking loops. An extreme example of the effect is the electric field just after the signal has traversed a single phase screen in a simulation. In this case, the signal amplitude is unchanged, but the phase may vary widely. If for the phase screen $\sigma_\phi >> 2\pi$, the plot of distribution of E is a circle of constant amplitude when plotted in terms of E_r, E_i, and $\overline{E}_r = 0 = \overline{E}_i$. In actuality there is, of course, no scintillation, although the autocorrelation function of E may have a very short decorrelation length.

Detrending can be approached from either the time or frequency domain of a receiver or equivalently from either the space or spatial frequency domain of the electric field in the receiver plane of a propagation simulation. The approach used here is that considering the spatial variation of the field vector. Detrending uses data from several points to estimate a mean value of the phase at some other point. The estimated mean is subtracted from the total phase and the remainder considered the random component of interest. In this way, one can attempt to isolate the large scale

phase fluctuations and the rapid random components due to multipath scintillations.

One must use some care in detrending. If the data points used to estimate the mean phase are too widely spread, there is little detrending action because the mean tends toward zero. On the other hand, if the points are too limited, the estimate of the mean may always be so close to the actual as to eliminate phase fluctuations. With such tight phase tracking, even a Rayleigh distribution can be converted to one which has a finite real average component. Unfortunately, it is difficult to predict what properties will lead to the best reduction of the data.

The detrend design used here operates with sampled data such as produced by the MPS calculation. For a particular sample variable y_n, the mean large scale component is taken to be

$$b_n = \sum_{-i_2}^{i_2} a_i \, y_{n+i} \tag{76}$$

and the detrended value of y is

$$y_n^* = y_n - b_n \quad . \tag{77}$$

The variation of the large scale component can be represented as a power series in i. If the detrend filter is desired to make y_n^* independent of the m^{th} power variation of the background,

$$\sum_{-i_2}^{i_2} i^m a_i = 0 \quad . \tag{78}$$

Thus, in principle, it is possible to make the detrend account for all power variations up to $2i_2$; however, because there is a random, noise-like component superposed on the slowly varying component, such a filter would be noisy.

For the current effort, the design has been such as to suppress powers through the third. The odd power components are eliminated if the a_i sequence is an even function (i.e., $a_i = a_{-i}$). Thus, we are left with the restrictions

$$\sum_{-i_2}^{i_2} a_i = 1 \tag{79}$$

$$\sum_{-i_2}^{i_2} i^2 a_i = 0 \quad . \tag{80}$$

It was also desired that the numerical implementation be simple and that the estimate of mean phase be independent of the measured value of the n^{th} sample.

The simplest detrend function meeting these requirements is that

$$\begin{aligned} a_0 &= 0 \\ a_i &= b_1 \qquad 0<|i|\leq i_1 \\ a_i &= b_2 \qquad i_1<|i|\leq i_2 \quad . \end{aligned} \tag{81}$$

This means

$$i_1 b_1 + (i_2 - i_1)b_2 = 0.5 \tag{82}$$

and

$$\sum_{i=1}^{i_1} i^2 b_1 + \sum_{i=i_1+1}^{i_2} i^2 b_2 = 0 \quad , \tag{83}$$

which can be rewritten as

$$i_1(b_1 - b_2) + i_2 b_2 = 0.5 \tag{84}$$

$$\sum_{i=1}^{i_1} i^2 (b_1 - b_2) + \sum_{i=1}^{i_2} i^2 b_2 = 0 \quad . \tag{85}$$

The expression for b_n can be similarly rewritten as

$$b_n = (b_1 - b_2) \sum_{i=-i_1}^{i_1} y_{n+i} + b_2 \sum_{i=-i_2}^{i_2} y_{n+i} - b_1 y_n \quad . \tag{86}$$

Parameters used in detrending to date are given in Table 1. This very simple detrend function was chosen for ease of implementation, rather than for any optimization of operational characteristics.

Table 1. Detrend filter parameters.

i_1	i_2	$b_1 - b_2$	b_2
5	10	0.140	-0.020
10	20	0.068333	-0.0091667
20	40	0.033750	-0.0043750
20	30	0.045898	-0.013932

Figure 4 shows a typical filter transmission function and the signal power spectral density for a single sample. The signal and filter responses were computed assuming the signal and filter weighting were constant between sample times. The transmission function shown, T(k), is the square of the Fourier transform of the spatial filter taking the unit distance to be the distance between samples. As can be seen, most of the signal power is where $|k| < \pi$. The filter shown is Detrend 5-10. Basically, the filter is matched to the signal but has both a sharp notch about k=0 and oscillations superposed on it. For larger values of i_1 and i_2, the notch becomes narrower (although the shape of it still is a k^8 relationship), the ripple frequency becomes greater and the ripple amplitude becomes less. The relative amplitude of the ripple is about $2(b_1 - b_2)$. If the filter factors a_i had been tapered to avoid discontinuities in the detrend filter, much of the ripple could have been suppressed.

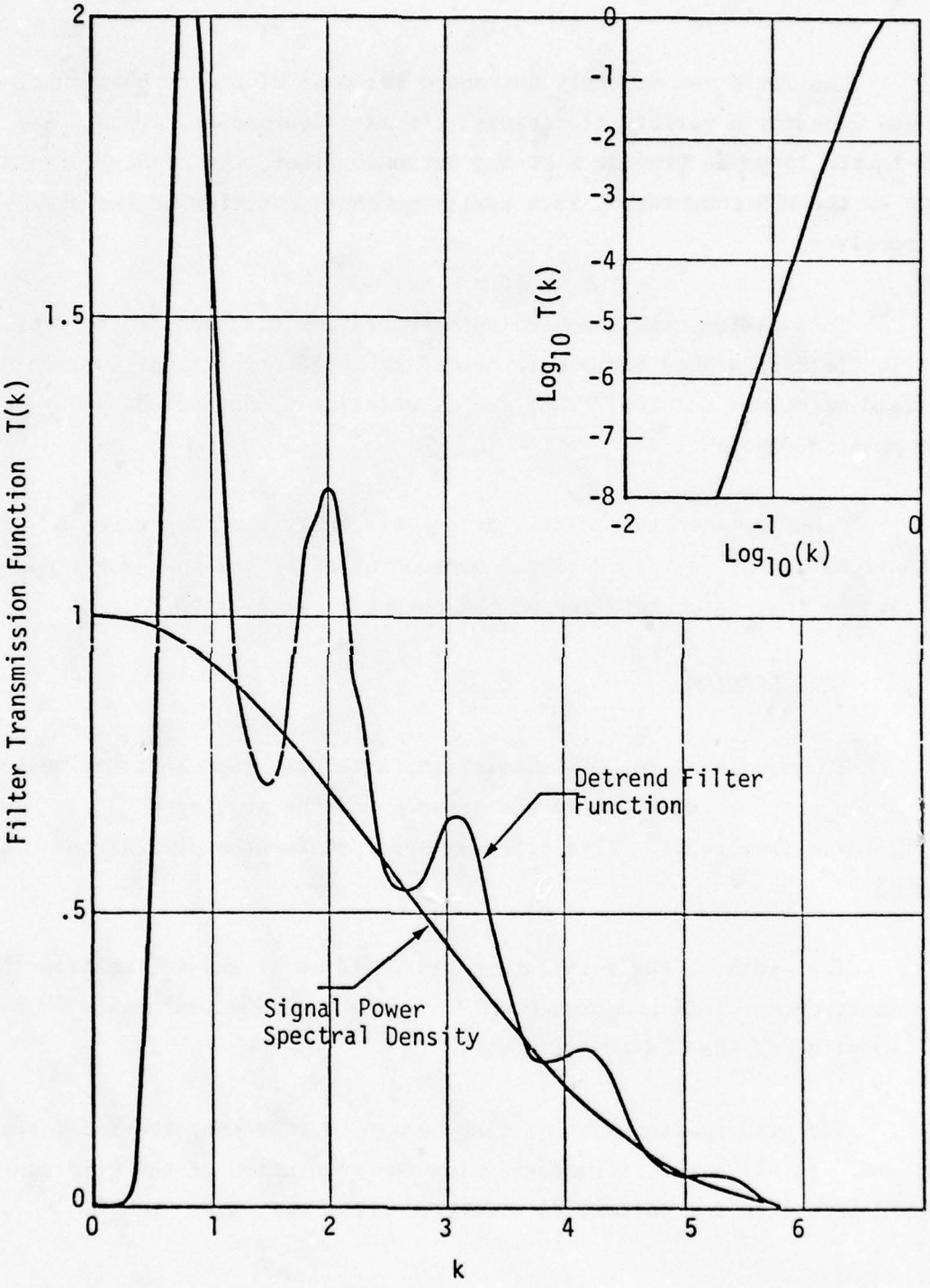

Figure 4. Frequency transmission function of detrend 5-10 filter.

The field was strongly detrended for most of the computations. This was done for a variety of reasons. In many equipments, the AFC and phase-locked loops do provide a strong detrend. Thus, the electric field output by the MPS computation is a realistic representation of the signal in a receiver.

In addition, the computed autocorrelation function of the detrended electric field is a good representation of the autocorrelation function of the field magnitude scintillations and is relatively unaffected by any large scale phase modulation.

Finally, when the scintillations are weak, the properties of the fluctuations in the detrended signal are dominated by the in-phase random component so that interpretation of the output is simplified.

4.3 GRID SPACING

In order that the MPS simulation faithfully represent the desired propagation problem, the size of the screens and the spacing of points must satisfy several criteria. Five criteria were met for the simulations reported.*

The width of the screens was chosen to be at least five times the phase shift decorrelation distance. This is to assure a reasonable statistical sampling of the phase distribution.

The grid spacing must be fine enough to represent the small scale structure. In all cases, structure below the resolution of the grid contributed less than one percent to effective phase variance.

---

*The derivation of the quantitative criteria are included in Reference 3.

It is also necessary that the phase representation be a reasonably continuous function. The specific criterion used was that the variation in phase shift between adjacent points in the grid represent less than a tenth of a wavelength.

The grid spacing must also be sufficiently fine that the maximum scattering angle be properly represented. Too great a grid spacing results in aliasing of energy in wrong directions. The spacing was required to be sufficiently fine to correctly propagate a wave at three times the standard deviation of the scattering angle. Thus, less than 0.1 percent of the energy could be aliased.

Because the problem was set up using an assumption of a cyclic screen with a basic period of the width of the phase screens, energy scattered out one edge of the screen reappears at the other. Consequently, to prevent the energy from a single point beating with itself in a coherent manner, the rms transverse deflection of a wave was limited to less than a tenth of the width of the phase screens.

4.4 CASES COMPUTED

Computations were performed for frequencies from 300 to 8000 MHz for rms electron concentration variations from 10^4 to 10^7 cm^{-3}. The striated media were taken to be both 500 km thick at a mean range of 1000 km and 150 km thick at a mean range of 300 km.

For the natural ionospheric model, the characteristic length ℓ was taken to be 0.42, 1.25, and 3.75 km. According to Wittwer[5], 1.25 km is typical of strongly disturbed natural equatorial ionospheres. These parameters furnished data for values of ℓ/ℓ_f from 0.38 to 35.

For the Chesnut model, ℓ was taken to be 0.3, 1.0, and 3.0 km. In addition, there was data available from previous computations[3] for an ℓ of 0.1 km. This provided values of ℓ/ℓ_f from 0.2 to 17.

Not all electron concentrations were run under all conditions because the small concentrations with high frequencies and long characteristic lengths result in no effect and large concentrations at low frequencies and short characteristic lengths result in Rayleigh distributions. In general, the computations at a particular combination of wavelength, characteristic length and mean range were carried out over a range of concentrations such that scintillation ranged from trivial to fully developed Rayleigh.

SECTION 5
RESULTS OF COMPUTATIONS

The results of the MPS computations are divided in the following sections into amplitude variations and field strength structure fading characteristics. Separate analysis of the data for each phase structure model is presented.

5.1 AMPLITUDE FLUCTUATIONS - NATURAL IONOSPHERE

Some typical data are shown in Figures 5 and 6. The distributions vary from one that exhibits very mild scintillations (a 3-dB fade occurring less than two percent of the time) to one that is essentially Rayleigh (greater than 10-dB fades ten percent of the time). The distributions for the cases of lesser disturbance can be fit reasonably well by gaussians except in the extreme tails of the distributions. The two straight-line approximations in Figure 5 are gaussians with variances obtained from the spatial autocorrelation function of the computed data.

The data for which $\sigma_\phi = 3.7$ radians and $\ell = 1.25$ km can be interpreted in terms of $\sigma^2_{eff}/\sigma^2_\phi$ both through the S_4 index and σ_r. Both yield the identical values of 3×10^{-3}, which is somewhat fortuitous. The data for which $\sigma_\phi = 2.2$ radians and $\ell = 0.42$ km can be interpreted through the S_4, σ_r, and the fading probability. These lead to values of $\sigma^2_{eff}/\sigma^2_\phi$ of 0.028, 0.029, and 0.029. The very good agreement indicates that the distribution is nearly Rician. However, this environment is still not very severe from the standpoint of the probability of deep fades.

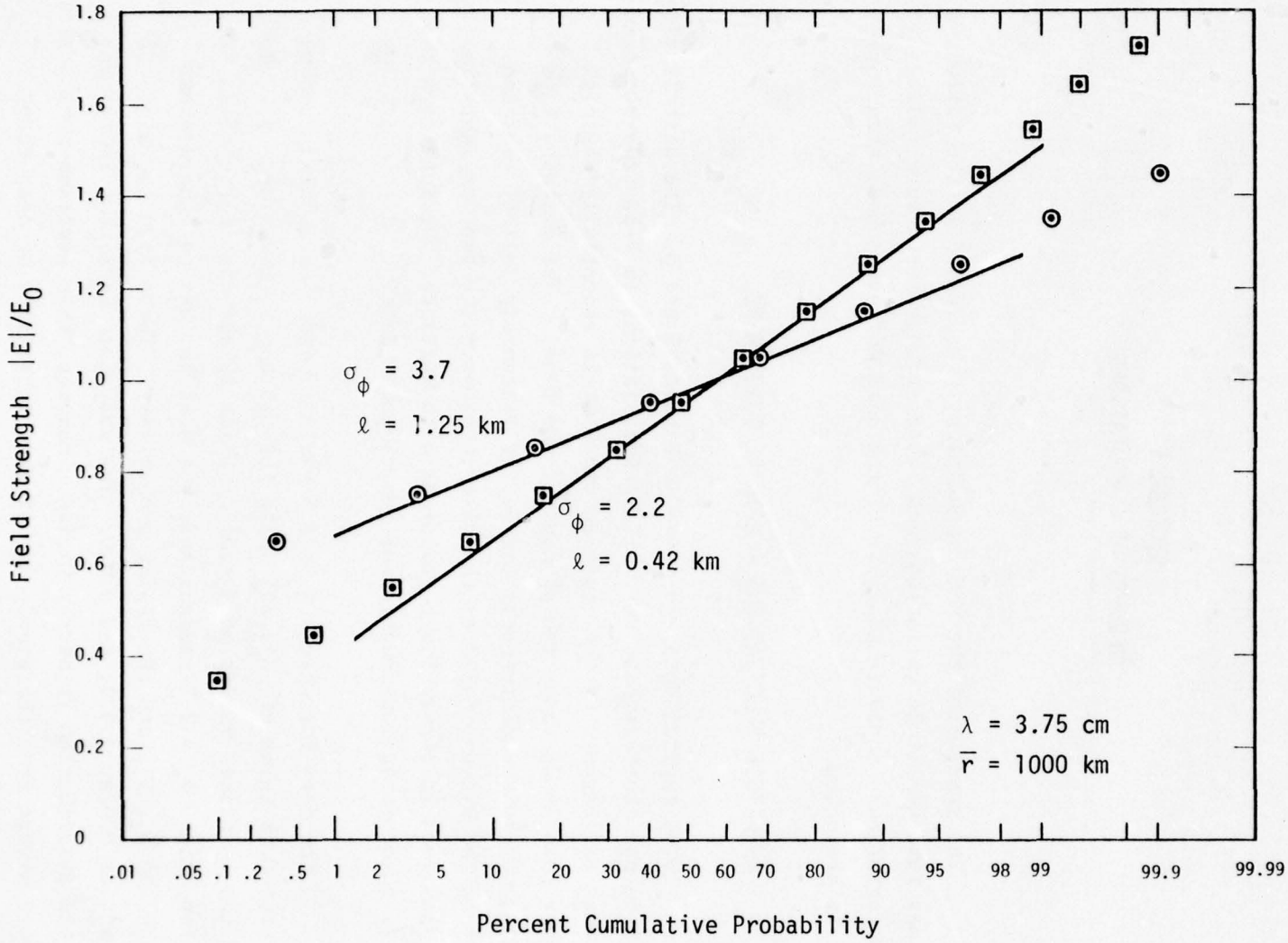

Figure 5. Field strength cumulative probability — natural ionosphere.

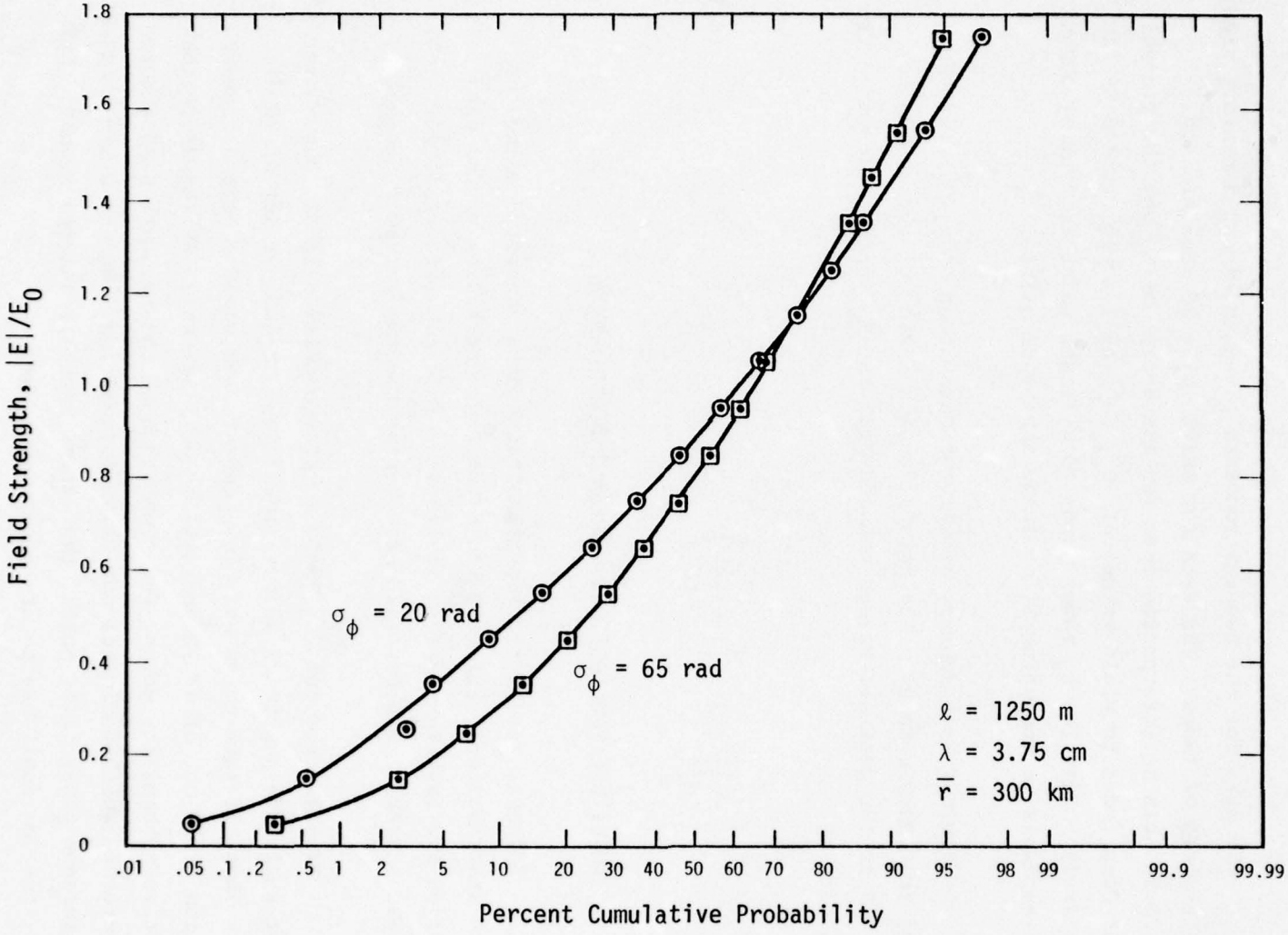

Figure 6. Field strength cumulative probability — natural ionosphere.

The data for the two environments given in Figure 6 exhibit significant numbers of fades. The data for which $\sigma_\phi = 20$ radians and $\ell = 1.25$ km can be interpreted from the standpoint of S_4 and the probability of deep fades to yield values of $\sigma^2_{eff}/\sigma^2_\phi$ of 1.4×10^{-3} and 0.85×10^{-3}, respectively. That the S_4 index leads to a larger value is typical because of the emphasis in computing S_4 of large amplitude points.

Figure 7 is a summary of all the data about $\sigma^2_{eff}/\sigma^2_\phi$ for the natural ionospheric model. The points about a factor of two above the curve fit to the data are values deduced from the S_4 index. The curve fit to the data is

$$\frac{\sigma^2_{eff}}{\sigma^2_\phi} = 1 - \left(1 + \frac{\ell_f^2}{4\ell^2}\right)^{-1/2} \quad . \tag{87}$$

5.2 AMPLITUDE FLUCTUATIONS — CHESNUT DISTRIBUTION

The next set of figures illustrates data generated using the Chesnut distribution. Figure 8 shows the reproducibility of the data. The two curves are each the average statistics of 20 separate realizations of the phase screens. The general character of the two curves is the same.

At the 1 percent (or 99 percent) probability level, the number of smaller amplitude points is 20 per simulation, or 400 per set of 20 simulations. Thus, if each point were independent, one would expect a standard deviation of 20 out of 4×10^4 points, or 0.05 percent. At the 99 percent cumulative probability point, the separation of the two curves is about ±0.1 percent, which indicates not great correlation. On the other hand, at the 1 percent probability point, the curves separate a large amount. Evidently, the low amplitude points occur in groups.

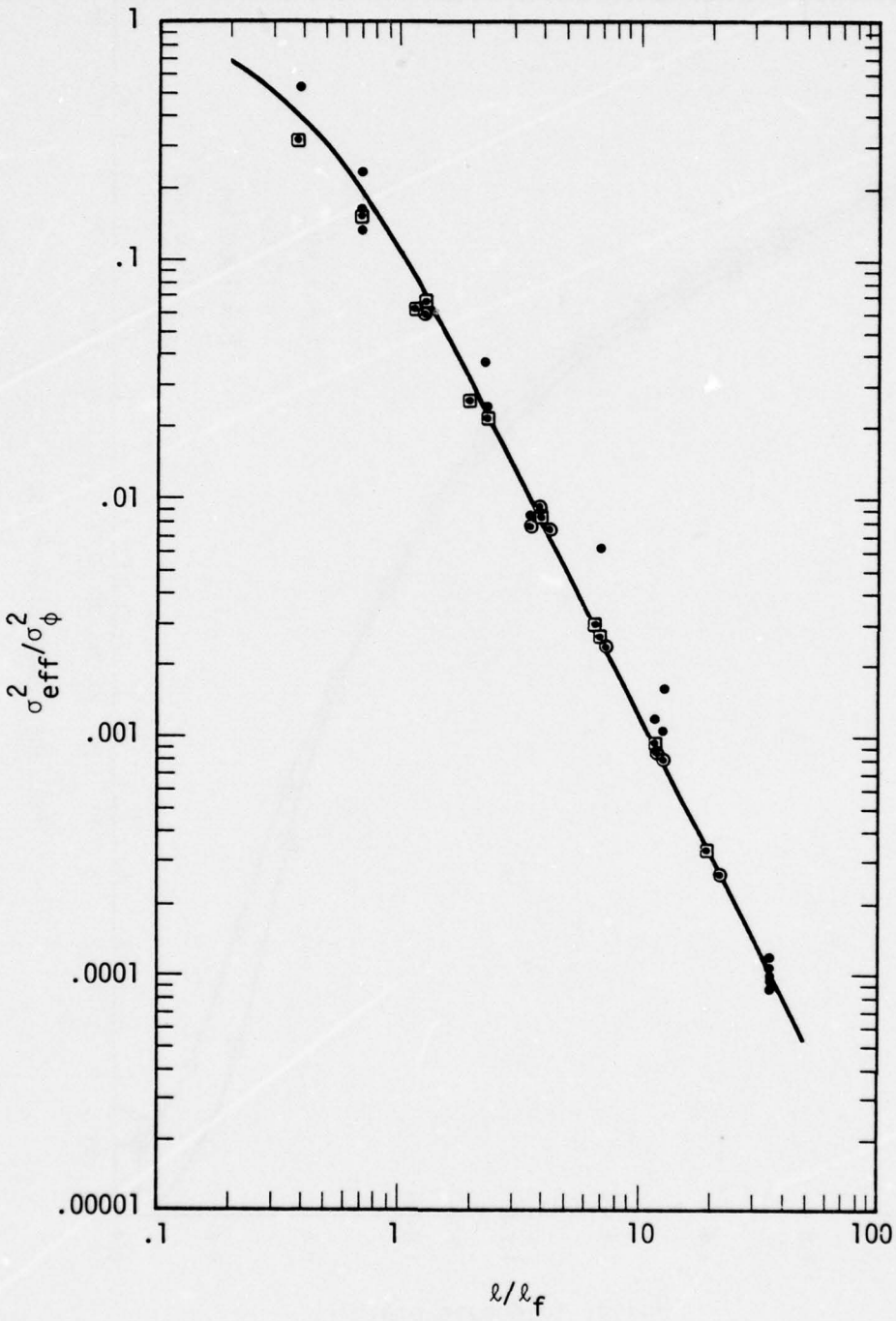

Figure 7. Effective phase variance — natural ionosphere.

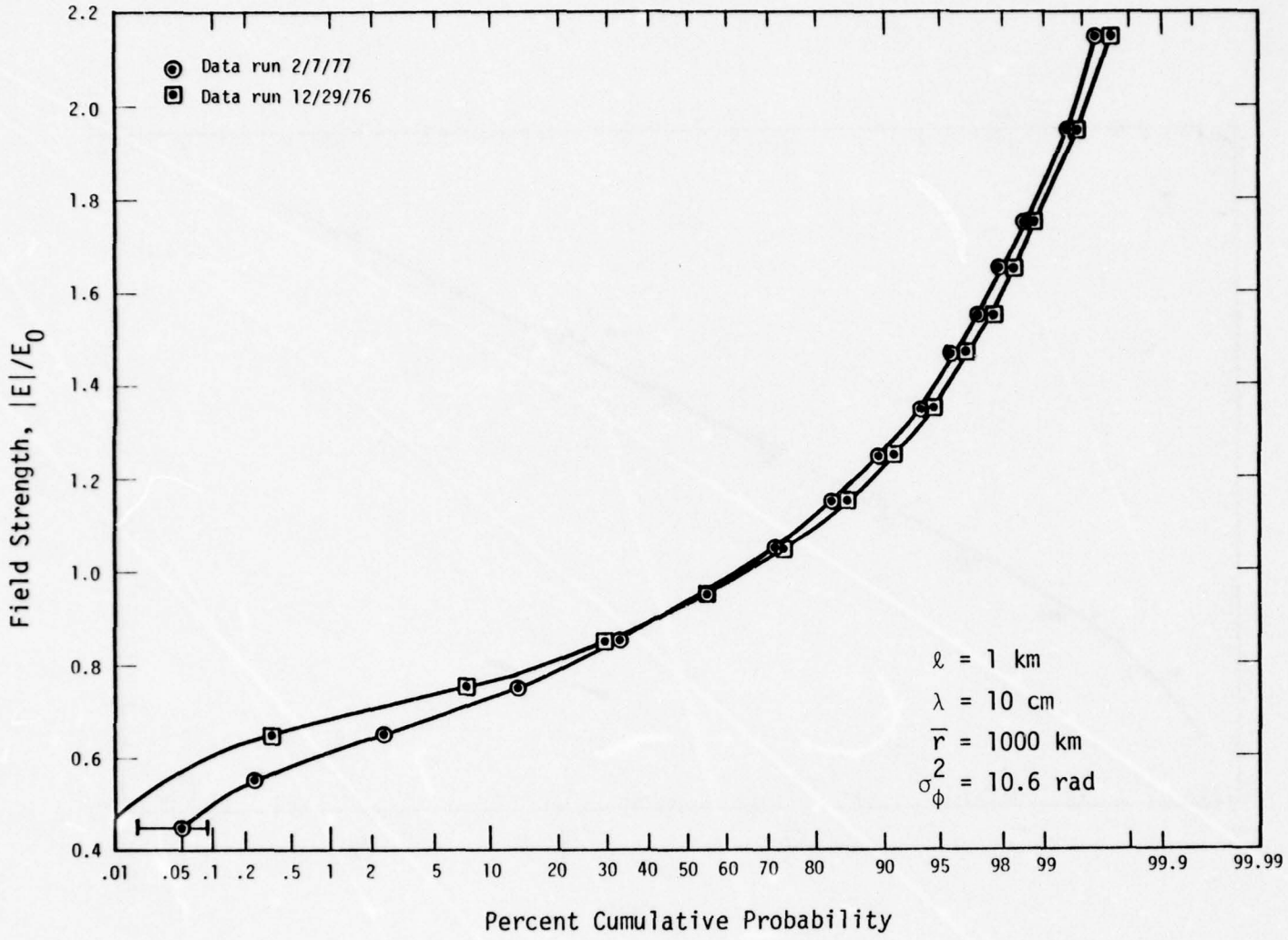

Figure 8. Field strength cumulative probability — Chesnut distribution.

The other significant characteristic of the curves is that they are decidedly not Rician. The probability of low amplitude points is about the same as for the data shown in Figure 5 for the natural ionospheric model with $\sigma_\phi = 3.7$, but the probability of electric fields more than 1.4 times the mean value is ten times greater — this is characteristic of data generated for the Chesnut model when ℓ is considerably greater than ℓ_f. Segments of the phase screen large compared to ℓ_f act as coherent lenses. In contrast, for the natural ionospheric model, there is sufficient small scale structure to break up the coherency from extended regions.

The development of the focusing is also shown in Figure 9. Here the increase in rms phase changes the low amplitude portion of the distribution function little, but the large amplitude portion markedly. The focal length associated with the rms value of the second derivative of phase shift is 1500 km for the screen for which $\sigma_\phi = 40$ radians. Inasmuch as the mean distance to the phase screens was 1000 km, it is not surprising that focusing was evident. The data making up this curve also had the property of an S_4 index in excess of 1 and a deep fading probability corresponding to a σ_ϕ of less than 0.3. Thus, for these curves, $\sigma^2_{eff}/\sigma^2_\phi$ depended to a greater extent on the type of data being interpreted.

Figure 10 shows some data for a smaller value of ℓ/ℓ_f. For this data, the low amplitude portion of the probability distribution is more nearly Rayleigh. For most systems we have studied so far, the most significant effect of scintillations is loss of signal during fades. For conditions such that fades are prevalent, the cumulative probability distribution function is nearly Rayleigh in the all-important low amplitude portions of the distribution. This is probably not too surprising because all it implies is that the two-dimensional probability density function in the complex plane is nearly constant in a region near the origin.

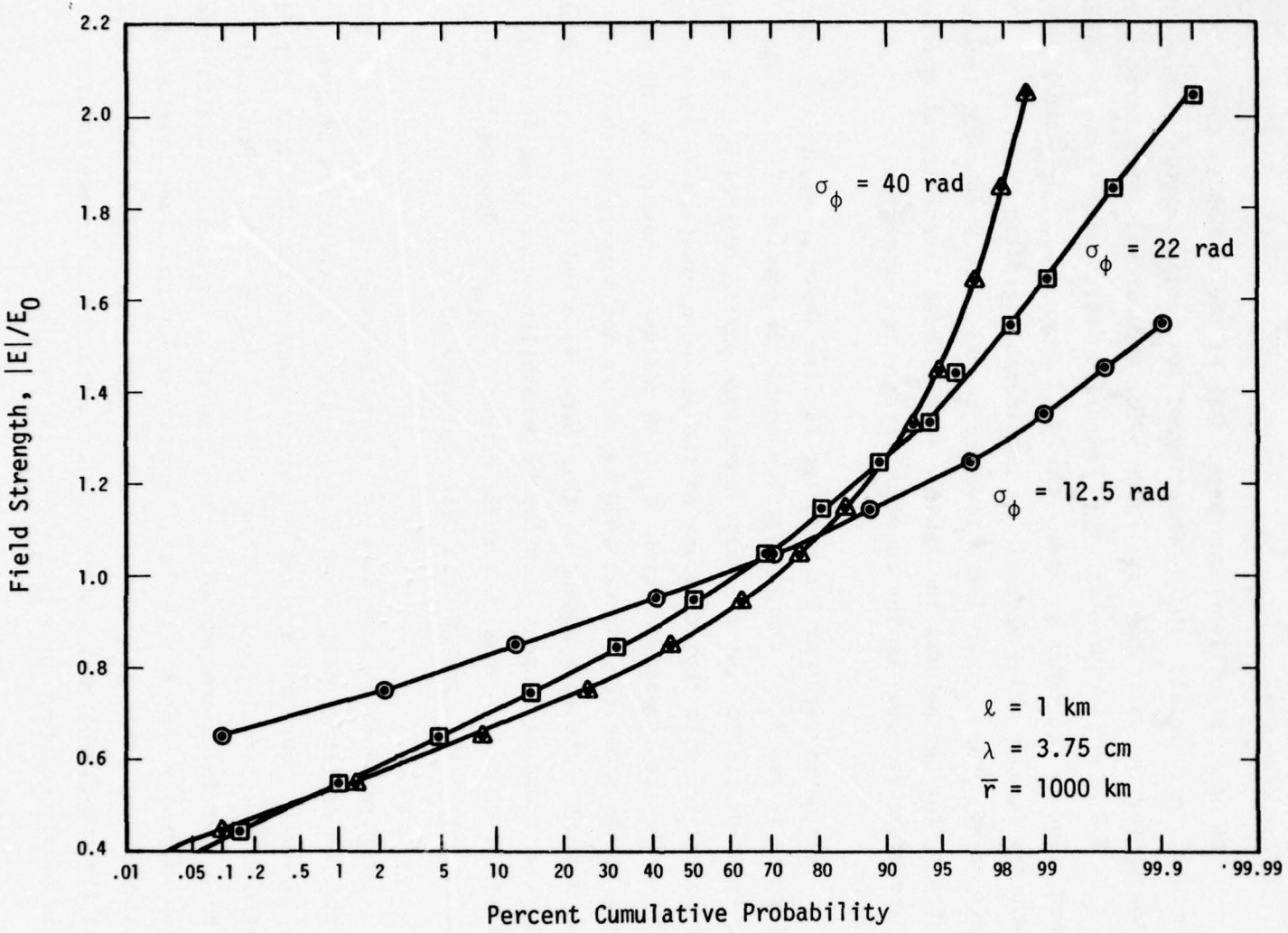

Figure 9. Field strength cumulative probability — Chesnut distribution.

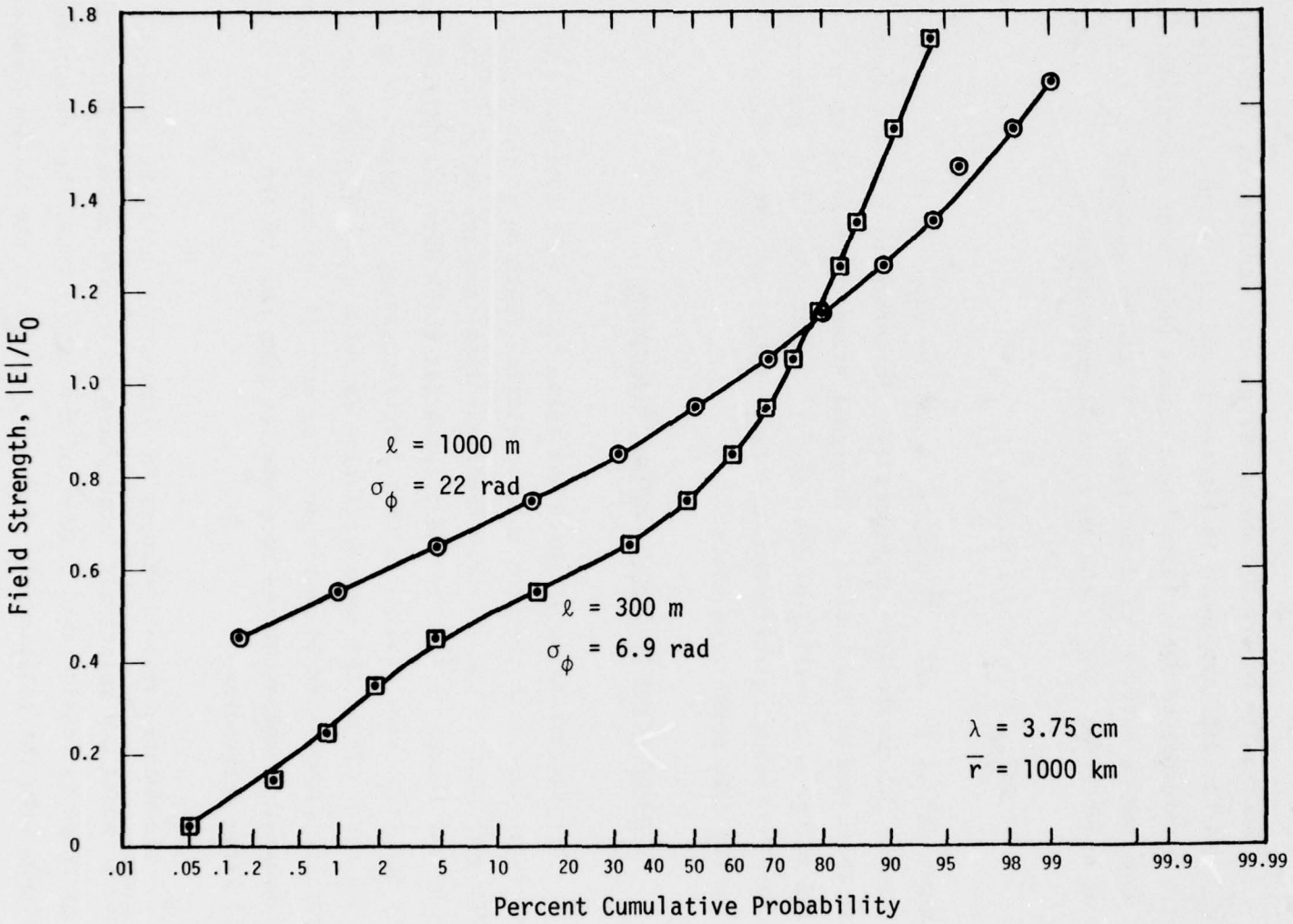

Figure 10. Field strength cumulative probability — Chesnut distribution.

The results of the MPS computations were interpreted in terms of $\sigma^2_{eff}/\sigma^2_\phi$ and the data are shown in Figures 11 and 12. Figure 11 includes all of the interpreted data; Figure 12 includes only those interpretations based upon the probability of deep fades. It can be seen that up to a value of about 3 for ℓ/ℓ_f, the data can be represented by

$$\sigma^2_{eff}/\sigma^2_\phi = \exp(-2.8\,\ell/\ell_f) \quad . \tag{88}$$

For larger values of ℓ/ℓ_f, the data exceed the exponential. A fourth power law is fit to the data in Figure 12. In Reference 3 it was shown that if the cause of the variation in signal strength is large scale focusing rather than multipath, the $(\ell/\ell_f)^{-4}$ relationship is appropriate. Thus, for the Chesnut distribution and large values of ℓ/ℓ_f, the observed trend in the data seems reasonable.

5.3 DECORRELATION DISTANCE — NATURAL IONOSPHERE

The decorrelation distance was taken to be that distance along the receiver plane such that the autocorrelation function of the random, in-phase component of the electric field was less than the value at the origin by the factor e^{-1}. In those cases for which data with different detrend functions were available, that function giving the tightest phase track was used. Thus, the autocorrelation function used was very close to that for the electric field magnitude. For most of the cases, the variance of the quadrature component was much smaller than that of the in-phase component, after detrending.

The decorrelation distances for simulations using the natural ionospheric model and relatively large phase shifts are shown in Figure 13. Although there is considerable scatter of the data points, they do cluster about lines with the relationship $\ell_d \propto \sigma_\phi^{-1}$, except at the smaller values of σ_ϕ. (The decorrelation distance for small values of σ_ϕ will be

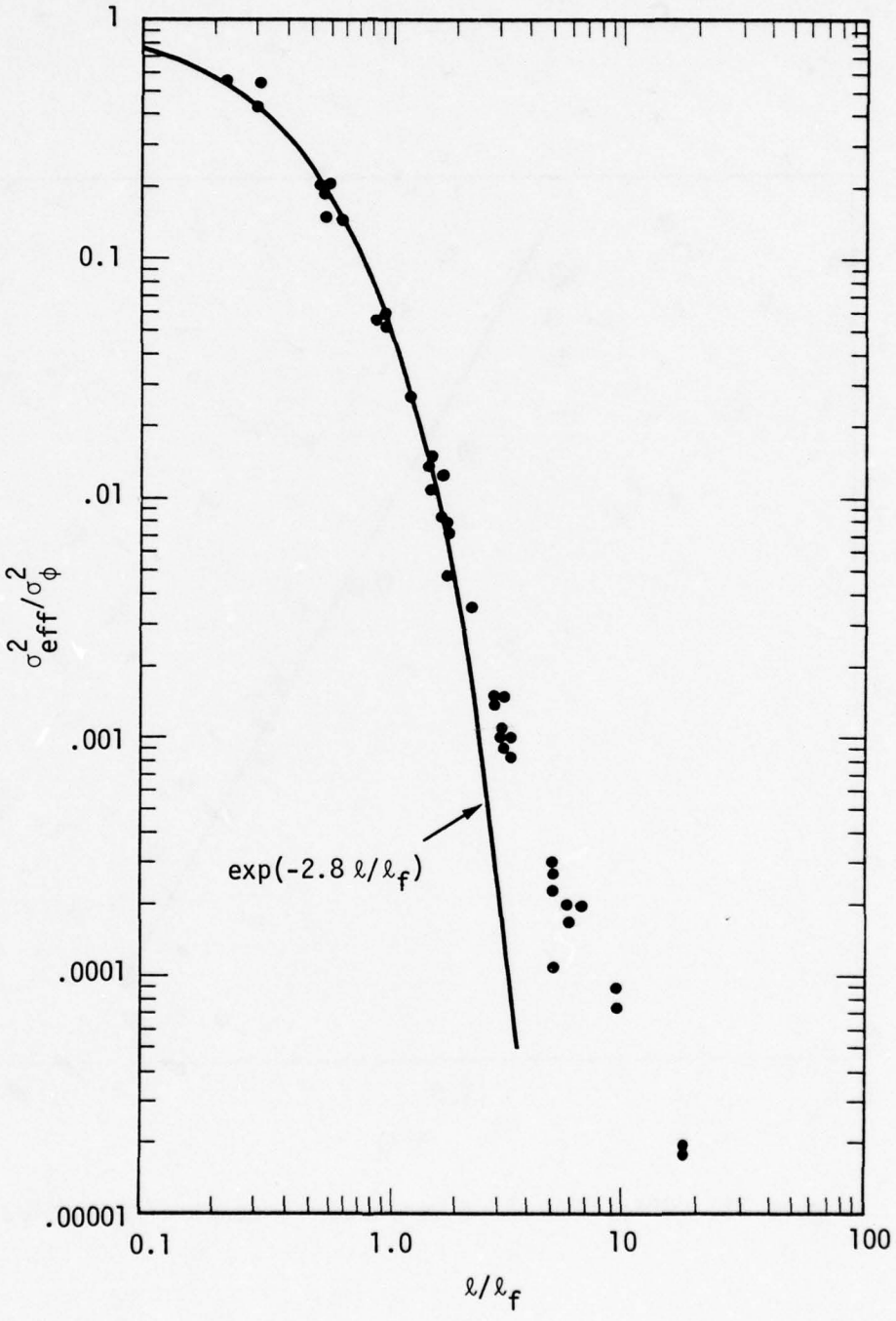

Figure 11. Effective phase variance — Chesnut distribution.

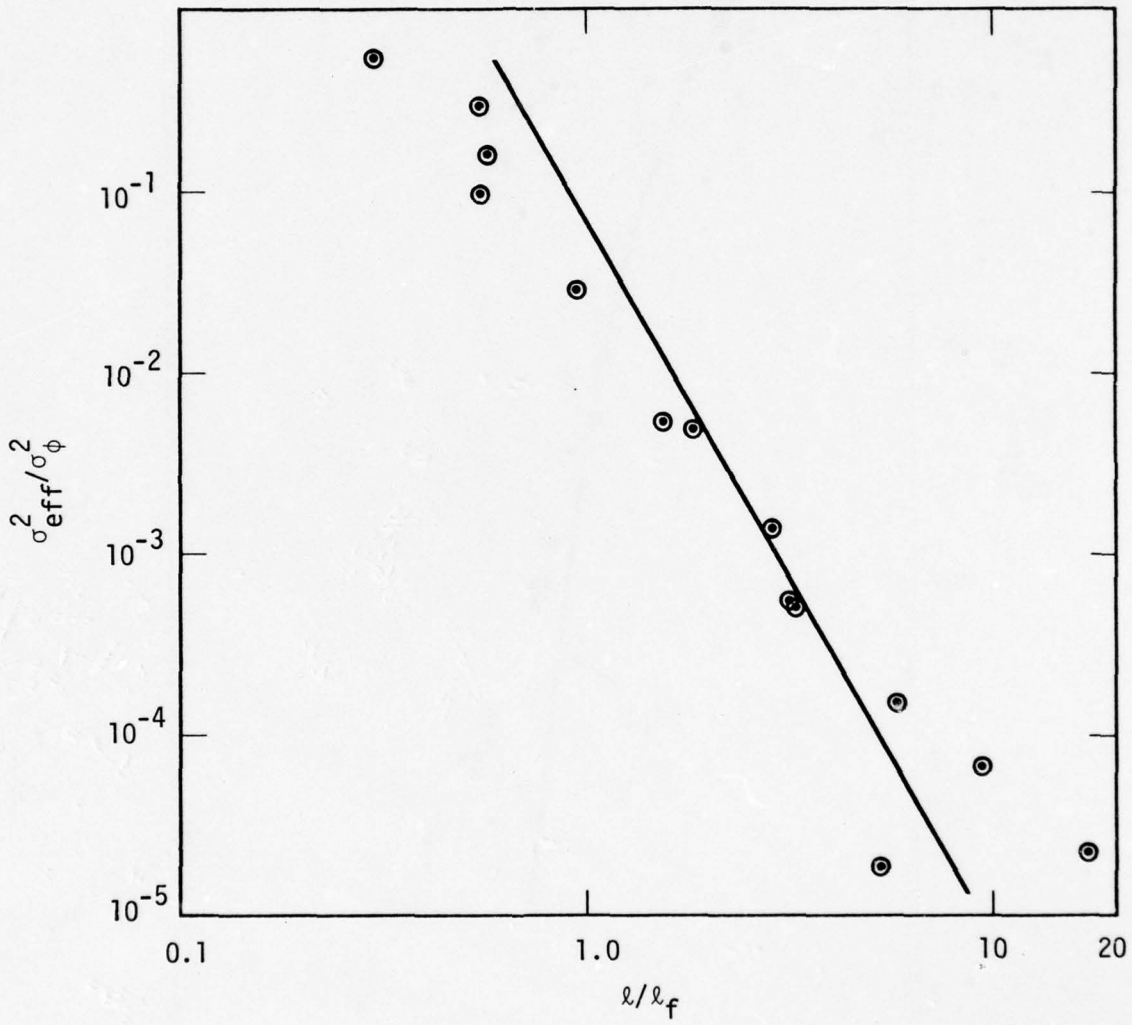

Figure 12. Effective phase variance — Chesnut distribution.

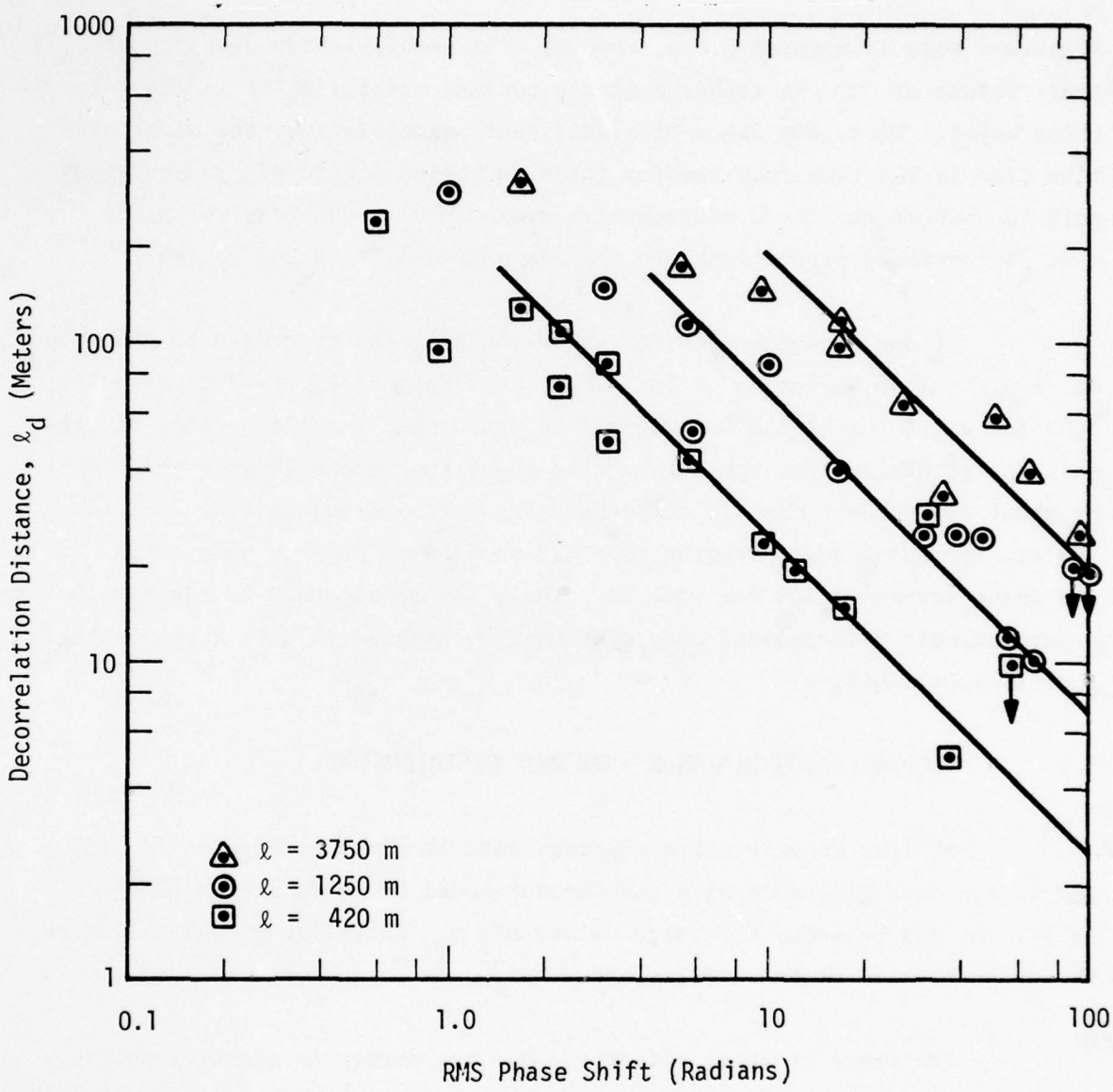

Figure 13. Decorrelation distance — natural ionosphere distribution.

discussed more in Section 5.5.) However, the decorrelation distance at small values of σ_ϕ is rather academic because scintillation is minor in those cases. Thus, for cases of significant scintillation, the decorrelation time is the time required for relative motion of the plasma and sight path to convect the field distribution a distance in the receiver plane that is inversely proportional to the rms phase shift of the screens.

If one uses the data for which the S_4^2 index exceeds 0.6, the value of $\ell_d\sigma_\phi/\ell$ is 0.58 for an ℓ of 420 m; 0.54 for an ℓ of 1250 m; and 0.55 for an ℓ of 3750 m. It should be noted that for these cases of significant scintillation, the data varied about the simple inverse power fit by about ±50 percent for all computed cases for wavelengths from 3.75 to 100 cm, for outer scale lengths from 420 to 3750 m, and for mean ranges to the phase screen of 300 and 1000 km. Thus, the data cannot be taken to be a particularly pathological case, but must be assumed to have a reasonably general applicability.

5.4 DECORRELATION DISTANCE — CHESNUT DISTRIBUTION

Similar decorrelation distance data is shown in Figures 14, 15, and 16 for data generated with the Chesnut model of phase screen phase shift. As can be seen, for large values of σ_ϕ (significant scintillation), the decorrelation distance falls off as σ_ϕ^{-1}.

The lines at small values of σ_ϕ are merely to identify points associated with nearly equal Fresnel distances (given in meters), which is a subject of discussion in Section 5.5.

The particular lines drawn for approximating the data for large scintillation cases are not best fits, but are the theoretical lines given by Equation 48, as will be discussed in Section 6.2. The best fitting lines with a slope of -1 are $\ell_d\sigma_\phi/\ell$ equal to 0.9 when ℓ = 100 m; equal to 1.32

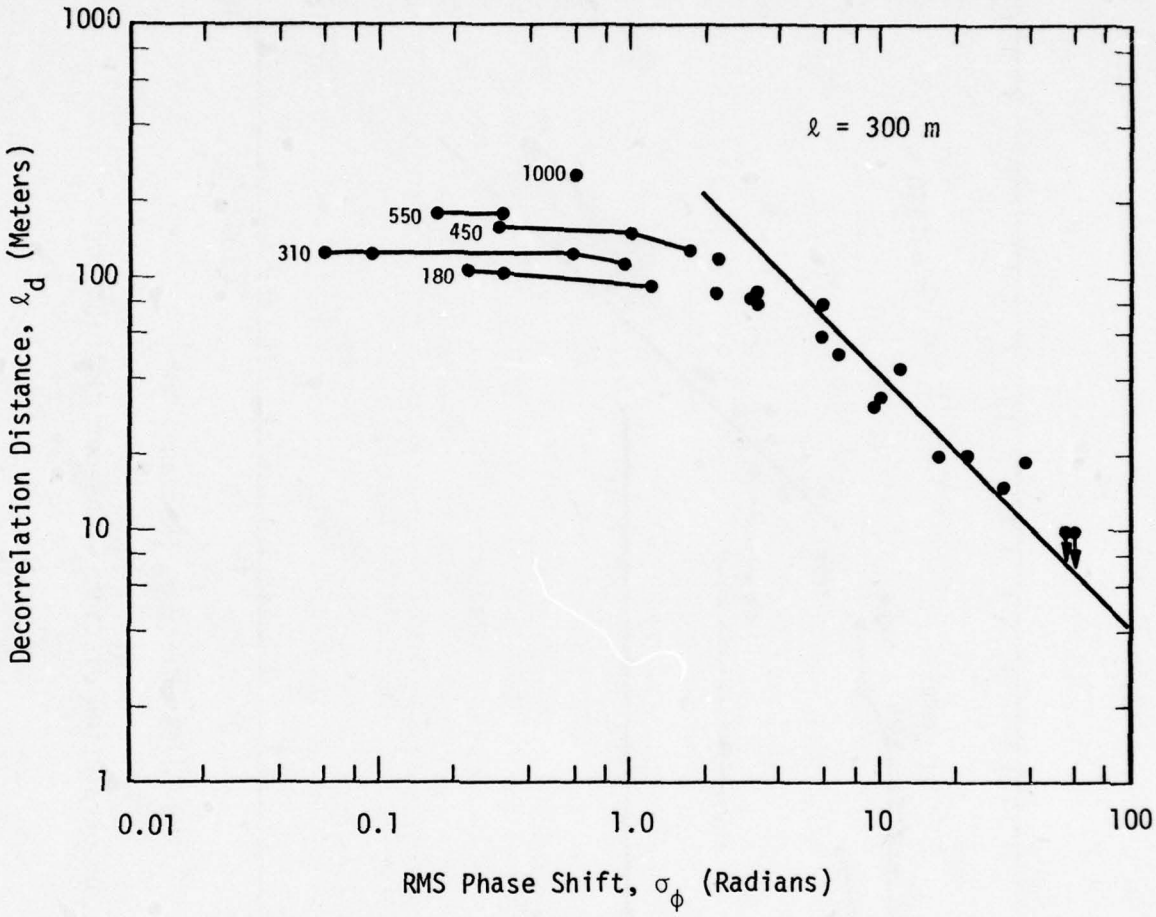

Figure 14. Decorrelation distance — Chesnut distribution.

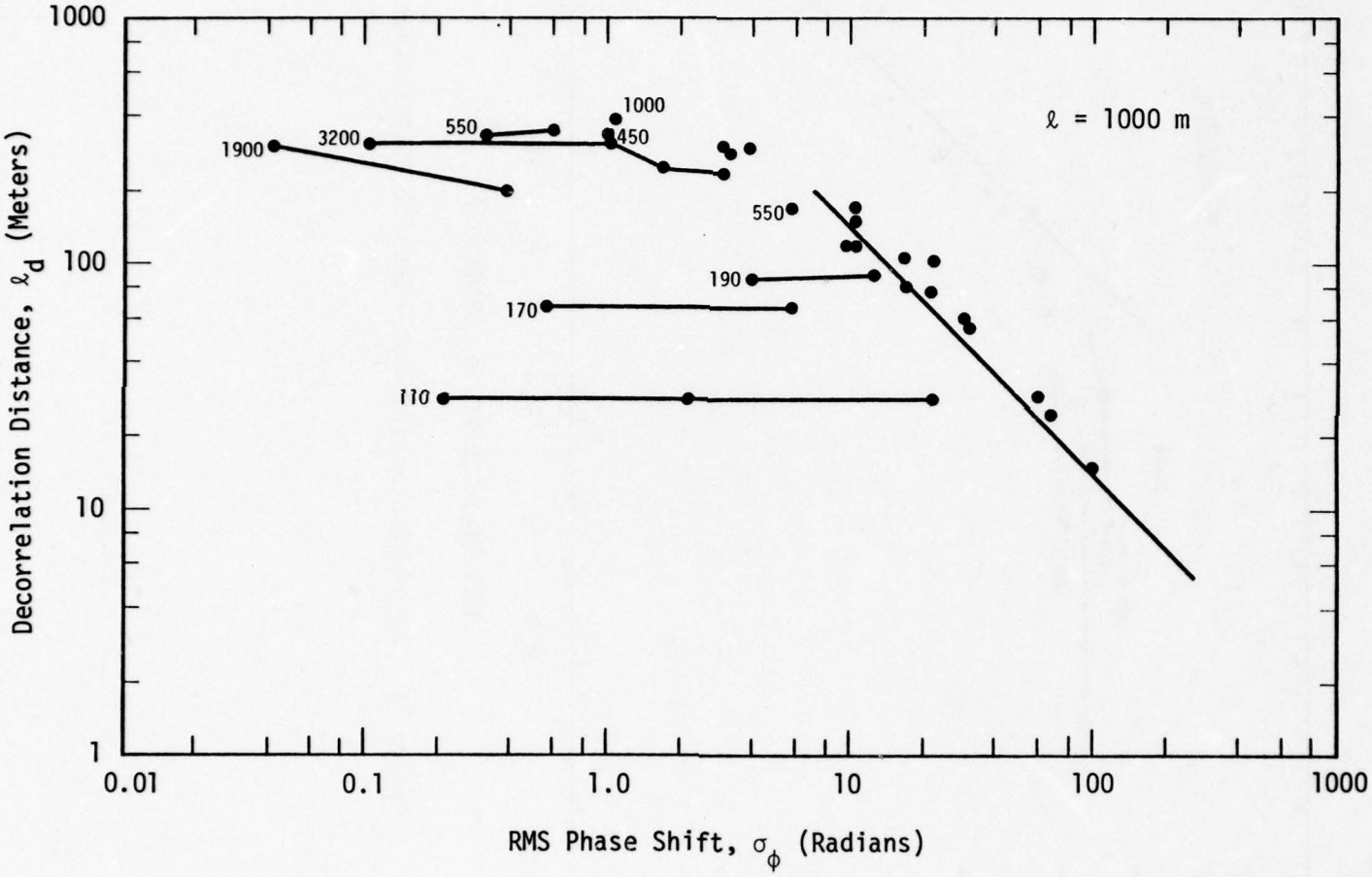

Figure 15. Decorrelation distance—Chesnut distribution.

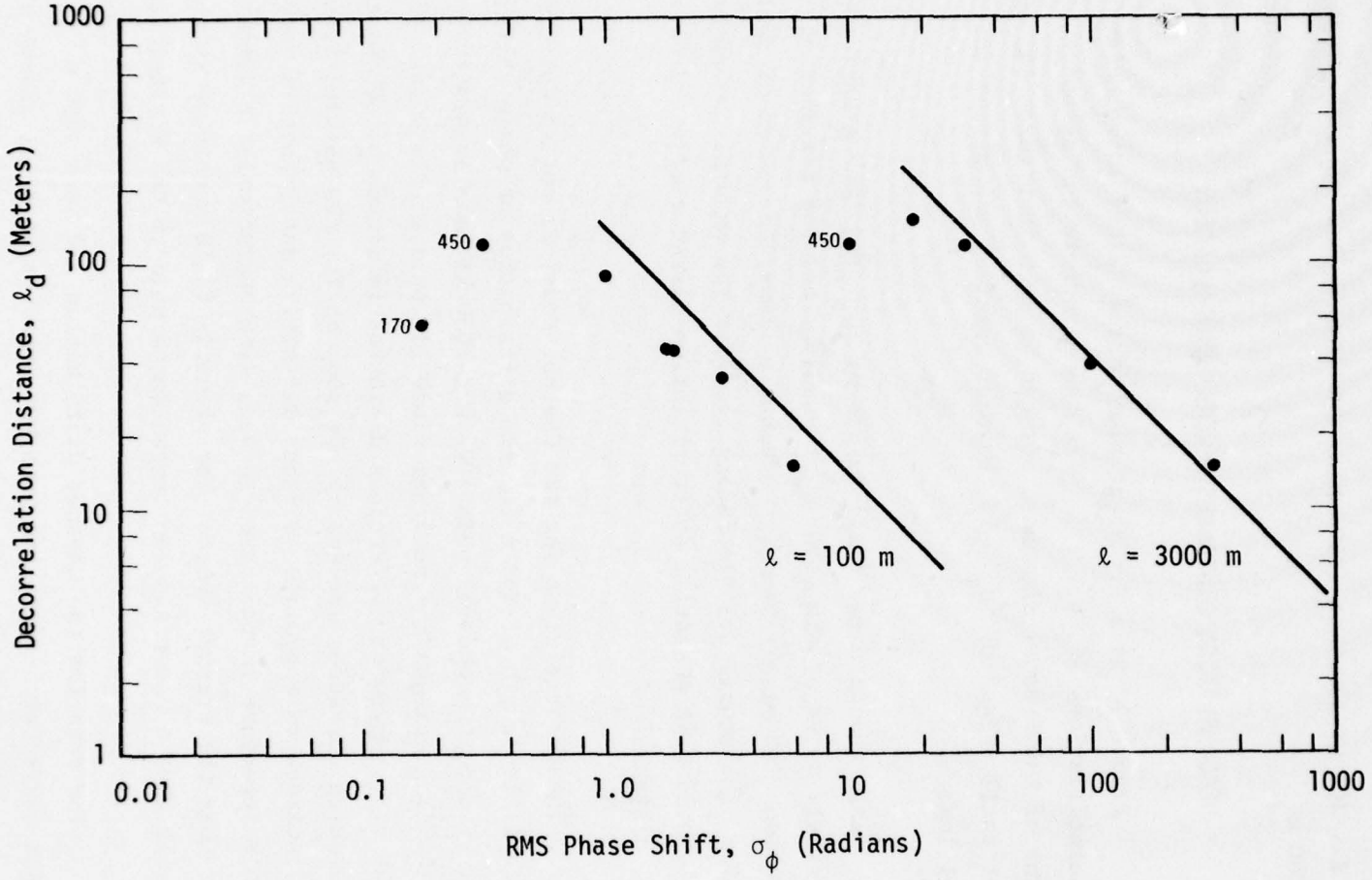

Figure 16. Decorrelation distance—Chesnut distribution.

when ℓ = 300 m; equal to 1.59 when ℓ = 1000 m; and equal to 1.38 when ℓ = 3000 m.

5.5 DECORRELATION DISTANCES — WEAK SCINTILLATION

Figure 17 is a different plot of the decorrelation distance for weak scintillations ($S_4^2 < 0.1$). Here the decorrelation distance is plotted in terms of the Fresnel distance. It can be seen in Figures 14, 15, and 16 that at small values of σ_ϕ, ℓ_d becomes relatively constant for a fixed Fresnel length.

All the data for small values of σ_ϕ for the natural ionosphere fit a single curve of the form $\ell_d = 0.324\,\ell_f$ and the variance of individual computations (42 cases) is only $0.018\,\ell_f$. Thus, for cases of small scintillation, the characteristic fading rate for the natural ionospheric model is associated with a spatial autocorrelation distance of a third of a Fresnel distance.

The decorrelation for the Chesnut model is not so uniform. For a characteristic length of 300 m for the distribution of phase shift, the data for all wavelengths and for both 300- and 1000-km mean separation of the phase shifting screens and receiver plane lie on a single curve with a slope of about 0.5. Moreover, at Fresnel distances in excess of 300 m, the decorrelation distances are nearly the same as for the natural ionosphere. One is inclined to speculate (without definitive data) that if there is considerable structure in the phase screens with characteristic dimensions smaller than the Fresnel length, the electric field magnitude in the receiver plane will show a decorrelation length comparable to the Fresnel length.

The data for the Chesnut distribution and ℓ = 1000 m displays a different character. It splits into two branches at small values of ℓ_f dependent upon the range to the phase shifting screens. For the screens at

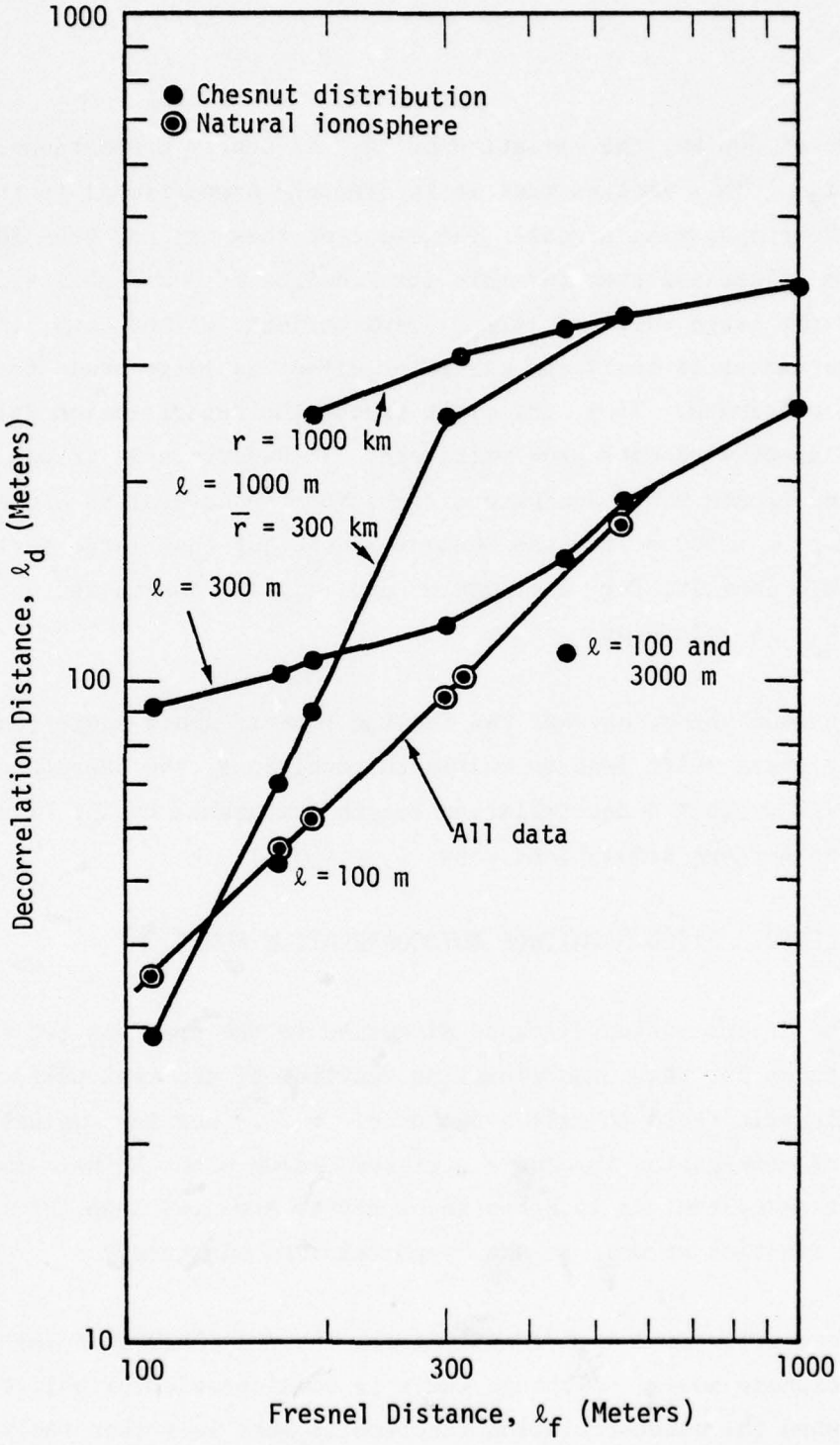

Figure 17. Decorrelation distance as a function of Fresnel distance for small phase fluctuations.

a mean range of 300 km, the variation of ℓ_d is nearly proportional to the square of ℓ_f. This implies that it is directly proportional to the wavelength of the propagating signal. The cause of this has not been identified. It should be reiterated that for this distribution of phase shifts in the screens and the large ratio of ℓ/ℓ_f characteristic of the data, the scintillation parameter is small and the major effect is large-scale focusing rather than multipath. Thus, one might expect the decorrelation distance to exceed that associated with true multipath. In Reference 3, it was estimated that multipath would dominate effects for the natural ionospheric model and for ℓ = 300 m for the Chesnut model, but that large-scale focusing would dominate for ℓ = 1000 m and $\sigma_\phi < 10$ (which is the region for which ℓ_d is independent of σ_ϕ).

In conclusion, one has the feeling that if small-scale fluctuations in the phase shift lead to multipath conditions, the detrended signal magnitude will exhibit a decorrelation length comparable to the Fresnel distance (the current simulations show $\ell_d = \ell_f/3$).

5.6 ELECTRIC FIELD MAGNITUDE AUTOCORRELATION FUNCTION

The decorrelation distance discussed in the previous two sections was the distance for the autocorrelation function of the real part of the detrended electric field to fall a factor of e^{-1} . For the evaluation of the effect of propagation through a striated medium upon the performance of a communication system, it is often necessary to know the shape of the autocorrelation function as well as the "decorrelation distance."

Some autocorrelation functions are shown in Figure 18 for the natural ionosphere model. Although there is considerable variability in the curves when the autocorrelation function is much less than the value at the origin (i.e., the normalized autocorrelation function is much less than unity), this portion of the autocorrelation function has very minimal

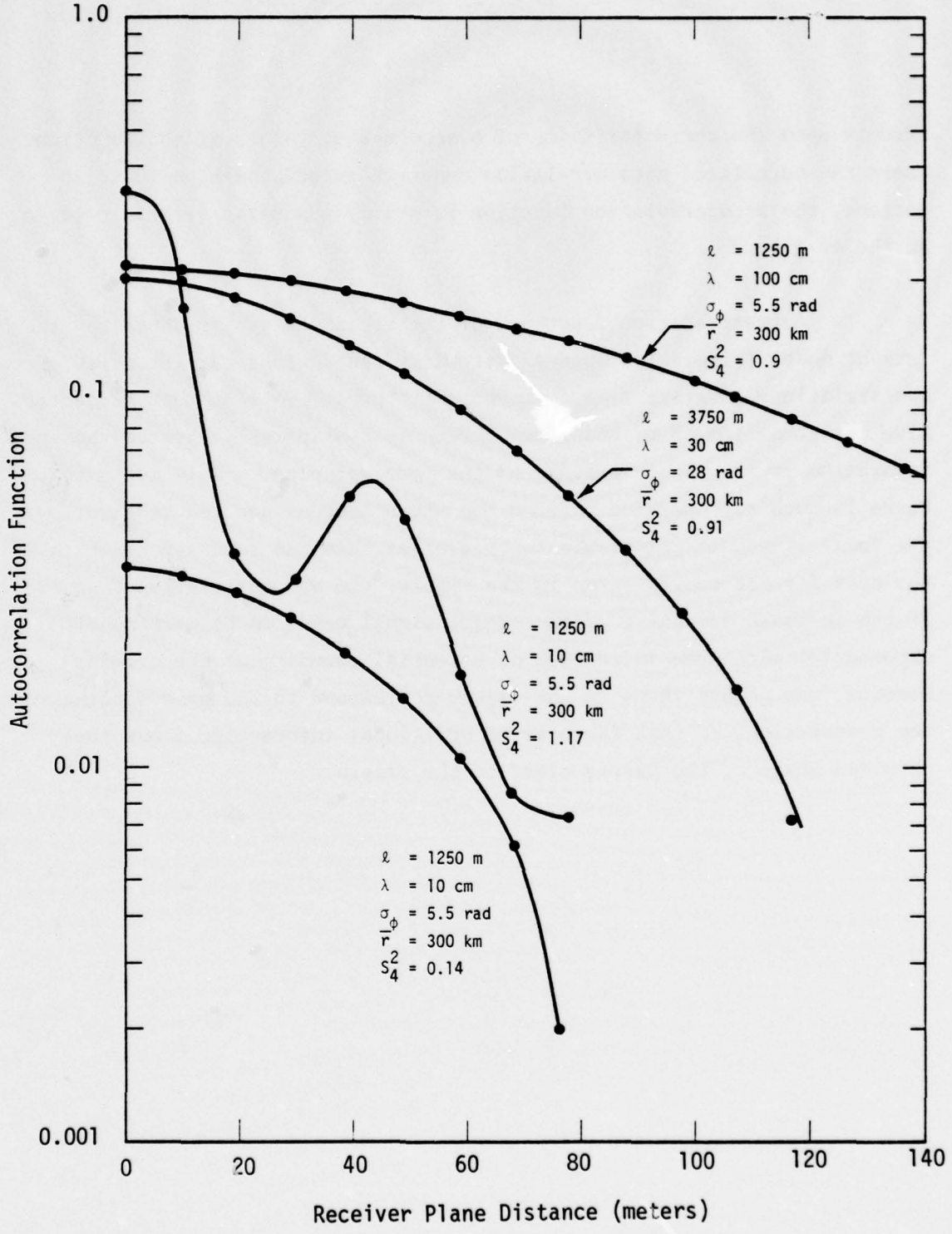

Figure 18. Autocorrelation function of detrended field strength — natural ionosphere.

effects upon the characteristics of a sequence of values of the function. Where the normalized autocorrelation function exceeds perhaps 10 to 20 percent, the autocorrelation function is nearly quadratic with zero slope at the origin.

Autocorrelation functions of the field strength produced by the Chesnut model (Figure 19) appear quite different unless the intensity of the striations is great. In this context, "great" implies that the effective rms focal length of the phase screen is considerably shorter than the separation of the phase screens and the receiver plane. This means that there is much ray crossing between the phase screens and the receiver. If the focal length is comparable to or greater than the separation, which is the case for the curves shown in the figure, the autocorrelation function of the in-phase component of the random signal tends to be more nearly exponential with some indication of potential rounding at the origin. However, the points shown in the figure correspond to the grid spacing in the computation, so that there is no additional information about the detailed shape of the curves close to the origin.

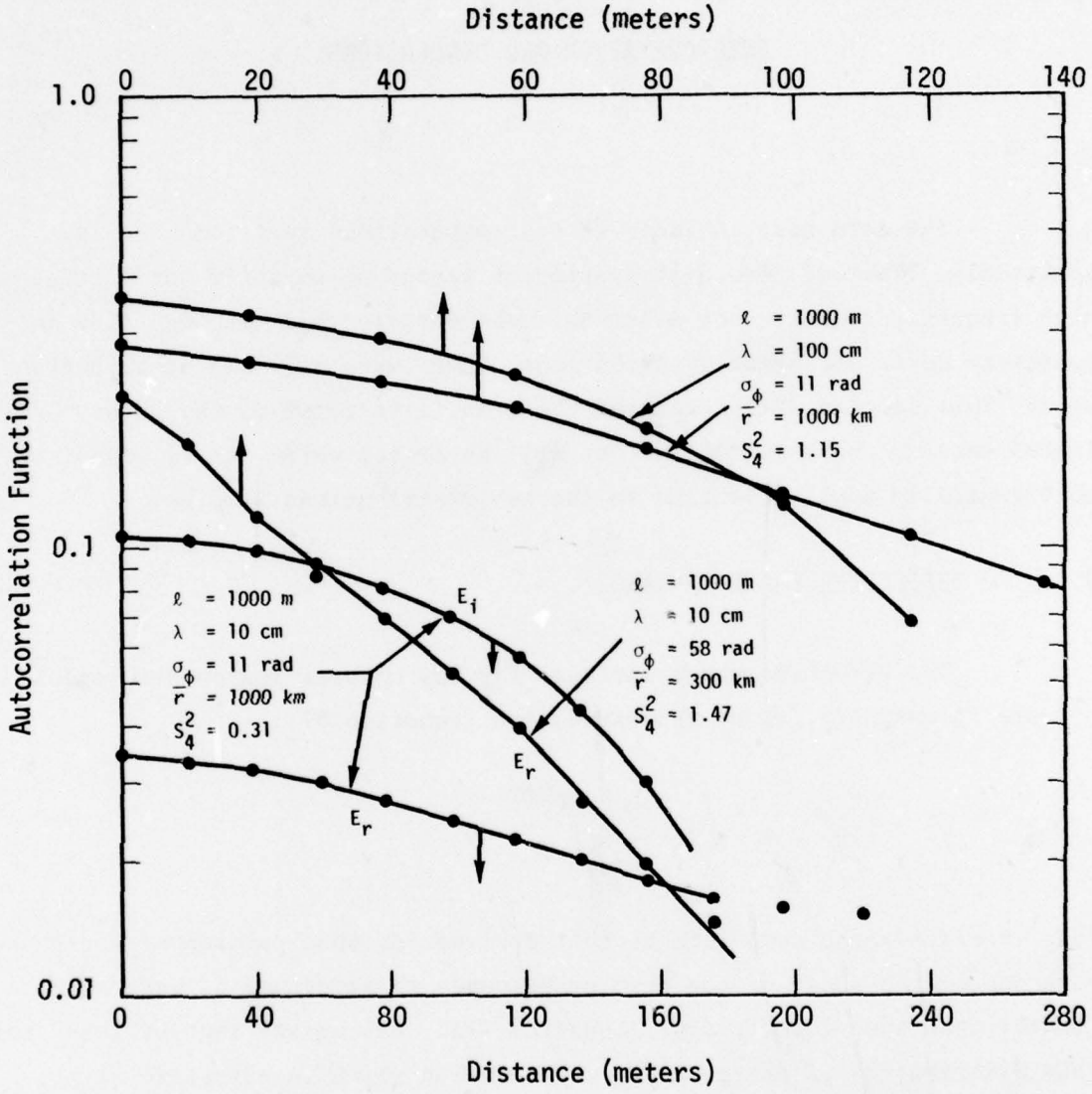

Figure 19. Autocorrelation function of detrended field strength — Chesnut distribution.

SECTION 6
INTERPRETATION AND CONCLUSIONS

The data base included in the computations reported here is, admittedly, limited. One distribution of random phase shift has little high frequency content, the other has considerable; but although they do represent quite different distributions, there were only two distributions used. This section will interpret the results in terms of the theory presented earlier and some conclusions will be stated which, it is hoped, are more generally applicable than to the two distributions studied.

6.1 EFFECTIVE PHASE VARIANCE

The effective phase variance for the natural ionospheric model (Figure 7) was well fit by the expression (Equation 87):

$$\frac{\sigma_{eff}^2}{\sigma_\phi^2} = 1 - \left(1 + \frac{\ell_f^2}{4\ell^2}\right)^{-1/2} \quad .$$

This is exactly the same form as that derived for that portion of the phase variance of the phase screen that corresponds to structure of wave number greater than some cutoff value (Equation 74). Let us say that at least for this distribution of phase shifts, the portion which is effective at producing scintillation is that finer than a particular limit. Call the wave number of this cutoff k_1 and the spatial wavelength λ_1 ($= 2\pi/k_1$) . If Equation 74 is normalized by dividing by the total σ_ϕ^2 and Equations 74 and 87 are compared, they become identical if

$$k_1 = 2/\ell_f \tag{89}$$

or

$$\lambda_1 = \pi\ell_f \quad . \tag{90}$$

If similar logic is applied to the Chesnut model data and Equation 88 (the experimental results) is compared to Equation 64, the result is identical to that for the natural ionospheric model, $\lambda_1 = \pi\ell_f$.

Thus, in cases of significant scintillation it seems reasonable to compute an effective phase variance associated with structure having a spatial wavelength shorter than $\pi\ell_f$, and to use this effective phase variance in the manner described for small scale structure in Reference 1. That is, the specular power is reduced over the free field power by

$$P/P_0 = \exp(-\sigma^2_{eff}) \tag{91}$$

and the remaining power is divided between in-phase and quadrature random components. Although the division is uneven for structure comparable in size to ℓ_f if scintillation is not too great, for cases of interesting degradation with some detrending device (AFC, for instance), little error should be introduced into simulations by taking the variances of the two components as equal.*

This result with reference to effective phase variance also implies that if the propagation medium extends over a long path length, then in the integration of the environmental parameters along the sight path one should compute the incremental effective phase variance for

---

*Some systems may be more sensitive to the division between random signal components than others. The actual numerical results from MPS calculations can be employed directly in receiver simulations to assess the sensitivity to variations in signal statistical properties.

segments of the path and sum them. Thus, the variation with distance of Fresnel distance and structural dimensions can be accounted for.

6.2 DECORRELATION DISTANCES

It is interesting to compare the measured decorrelation distances with the theoretical values far from the phase screen as given in Equation 48 ($\ell_d = \sqrt{2}/\sigma_{\phi'}$) . For the natural ionospheric model, Equation 67 relates σ_ϕ and $\sigma_{\phi'}$:

$$\sigma_{\phi'}^2 = \frac{\sigma_\phi^2}{\ell^2} \ell n(2k_m \ell) \quad . \tag{92}$$

Inserting the value of the inner scale wavelength λ_m in terms of the inner scale wave number yields

$$\frac{\ell_d \sigma_\phi}{\ell} = \left(\frac{2}{\ell n(4\pi \ell/\lambda_m)} \right)^{1/2} \quad . \tag{93}$$

The appropriate value to use for λ_m is unclear. The description of the MPS simulation (Reference 5) implies that it is about 20 m. If it were shorter than that, the highest frequency structure would not be represented in the simulation because most cases used a grid spacing of 10 m. If one requires two points per cycle (necessary to avoid aliasing), λ_m once again comes out to be about 20 m. If this minimum wavelength were in error by a factor of two, it would make a difference of only 6 percent in the theoretical value of $\ell_d \sigma_\phi/\ell$. Table 2 shows the experimental value for the mean value of $\ell_d \sigma_\phi/\ell$ using data for which $S_4^2 > 0.6$ and also shows the theoretical values using $\lambda_m = 20$ m .

The theoretical and experimental values are sufficiently close that one feels reasonable confidence in computing ℓ_d in this manner. It is interesting that from the standpoint of the decorrelation distance, it is the

total value of σ_ϕ that is important, not the effective value. The reason, of course, is the use of only that data associated with large amounts of scintillation. The effective σ_{eff} determines when scintillations start, but once they have started, multipath occurs for rays converging according to the total $\sigma_{\phi'}$. Actually the straight-line fits with unit slope in Figure 13 are the theoretical curves and can be seen to represent the data well within the scatter of individual points.

Table 2. Normalized decorrelation distances for cases of significant scintillation—natural ionosphere.

ℓ (meters)	Experimental	Theoretical
420	0.575 ±0.038	0.60
1250	0.543 ±0.028	0.55
3750	0.55 ±0.048	0.51

What is the case for the Chesnut distribution? In that set of computations $\sigma_{\phi'}$ is just σ_ϕ/ℓ (Equation 62) . Thus, theoretically

$$\frac{\ell_d \sigma_\phi}{\ell} = \sqrt{2} \quad . \tag{94}$$

This was used to determine the fit to the data in Figures 14, 15, and 16. The fit is within 10 percent, except for the data for which $\ell = 100$, where experimentally $\ell_d \sigma_\phi/\ell$ is 0.9 rather than 1.4 .

It certainly appears reasonable to approximate the decorrelation distance by $\sqrt{2}/\sigma_{\phi'}$ unless additional research indicates otherwise.

6.3 SHAPE OF AUTOCORRELATION FUNCTION

For the phase screens that appear to give true multipath in the sense of many interfering rays (the natural ionosphere), the spatial autocorrelation function has zero slope and is concave downward at the origin. This leads to well behaved spatial derivatives of the electric field (and well behaved time derivatives as it convects past a receiver). As the time intervals between samples of the signal decrease, the time derivative of the signal becomes constant, so that the change in the signal becomes proportional to the time interval.

In contrast, for some cases, the Chesnut model leads to nearly exponential autocorrelation functions. This can be explained in terms of ray optics. The large scale focusing associated with the lack of high spatial frequency components in the phase screen results in optical caustic curves. Across such a caustic, the electric field may change rather abruptly. It is such discontinuities in the field that can lead to an autocorrelation function which has a non-zero slope and an indeterminate curvature at the origin.

In actual practice, diffraction should limit the abruptness of changes across the caustics and hence round off the autocorrelation function at the origin. Even in the worst set of data shown (the data in Figure 19 for which ℓ = 1000 m, λ = 10 cm, σ_ϕ = 58 rad, and $\overline{r}$ = 300 km), there is a hint of this round off. There is one more effect that rounds off the autocorrelation function. The signal actually detected by the receiver has an autocorrelation function which is the convolution of the field strength autocorrelation function and the antenna aperture.

It is the feeling of the author that it is unlikely that an actual distribution of phase shifts will be so deficient in high spatial frequency components as the Chesnut distribution and in fact that there will always

be a region near the origin where the autocorrelation function can be fit by a concave-downward quadratic.

6.4 SUMMARY

6.4.1 Effective Phase Shift

The environmental phase shift effective in producing scintillation in microwave satellite communication systems can be obtained from the PSD of the integrated phase fluctuation

$$\sigma^2_{eff} = \int_{2/\ell_f}^{\infty} PSD_\phi \, dk \quad . \tag{95}$$

This phase shift variance can then be used as though it came from structure small compared to the Fresnel zone.

6.4.2 Decorrelation Distances

The decorrelation distance of the electric field in the receiver plane is

$$\ell_d = \sqrt{2}/\sigma_{\phi'} \tag{96}$$

if scintillations are significant. ($\sigma^2_{\phi'}$ is the variance of the transverse derivative of integrated phase in the environment.)

6.4.3 Shape of Autocorrelation Function

For the natural ionospheric model and for many conditions for the Chesnut model, the autocorrelation function is well represented by a downward open parabola with a width commensurate with the decorrelation distance. In some cases, for the Chesnut model, large scale focusing leads to

caustic curves and an autocorrelation function which is parabolic over a limited region and then becomes exponential.

6.4.4 Wavelength Dependence of Effects

It is interesting to compare the value of the variance of the local electron concentration fluctuations necessary to produce a given level of signal scintillation (i.e., the onset of major scintillations). If $\ell > \ell_f$, the effective phase variance is proportional to $\sigma_\phi^2 \ell_f^n$, where n is about 2 for the natural model and 4 for the Chesnut model. Thus, for a particular value of σ_{eff}^2, $\sigma_\phi^2 \propto \ell_f^{-n}$; also, $\ell_f \propto \lambda^{1/2}$, so that the needed $\sigma_\phi^2 \propto \lambda^{-n/2}$. On the other hand, for a fixed environment $\sigma_\phi^2 \propto \lambda^2 \sigma_{n_e}^2$. The final implication is, then, that to produce a given level of scintillation requires a local electron concentration variance that depends upon λ^{-3} for the natural ionospheric model and λ^{-4} for the Chesnut. However, at the onset of scintillations, the fading rate will be faster at the shorter wavelengths because the total σ_ϕ will be greater.

6.4.5 Research Requirements

In order to evaluate satellite communication systems with precision, it is necessary to develop the capability of performing the integral of Equation 95. Thus, the PSD of the integrated environmental phase shift must be available at least at spatial wavelengths less than typical Fresnel zones. Current weapons effects phenomenology does not provide this information.

Another reason for needing the research to determine the PSD is to allow a more definitive choice between the parabolic and exponential spatial autocorrelation functions in the receiver plane. (Although even for the Chesnut distribution, only a limited range of problem parameters leads to exponential autocorrelations.)

REFERENCES

1. Hendrick, R. W., Jr. and L. Shaeffer, Propagation in Striated Media, DNA 4019T, MRC-R-118, Mission Research Corporation, May 1976.

2. Hendrick, R. W., Jr., Striation Induced Fading Rates, MRC-N-151, Mission Research Corporation, October 1974.

3. Hendrick, R. W., Jr., Propagation Analysis for GPS, II/1-M-147, MRC-R-307, Mission Research Corporation, April 1977.

4. Bogusch, R. L., et al., HARC: A Detailed Simulation of Radar Tracking Measurements in a High Altitude Nuclear Environment, MRC-R-32, Mission Research Corporation, July 1972.

5. Wittwer, L.A., T. Salvi, and E. Pettus, UHF Propagation Effects in Scintillated Environments, AFWL-TR-76-304, Air Force Weapons Laboratory, August, 1977.

DISTRIBUTION LIST

DEPARTMENT OF DEFENSE

Assistant Secretary of Defense
Cmd. Cont. Comm. & Intell.
ATTN: M. Epstein
ATTN: J. Babcock

Director
Command Control Technical Center
ATTN: C-650, G. C. Jones
ATTN: C-312, R. Mason
ATTN: C-650, W. Heidig

Director
Defense Advanced Rsch. Proj. Agency
ATTN: Nuclear Monitoring Research
ATTN: Strategic Tech. Office

Defense Communication Engineer Center
ATTN: Code R820, R. L. Crawford
ATTN: Code R410, James W. McLean

Director
Defense Communications Agency
ATTN: Maurey Raffensperger
ATTN: Code 480
ATTN: Code 810, R. W. Rostron
ATTN: Code 101B, Maj Rood

Defense Communications Agency
WWMCCS Systems Engineering Org.
ATTN: R. L. Crawford

Defense Documentation Center
12 cy ATTN: TC

Director
Defense Intelligence Agency
ATTN: DT-1B
ATTN: W. Wittig, DC-7D

Director
Defense Nuclear Agency
ATTN: TISI Archives
ATTN: STVL
3 cy ATTN: TITL Tech. Library
ATTN: DDST
3 cy ATTN: RAAE

Commander
Field Command
Defense Nuclear Agency
ATTN: FCPR

Director
Interservice Nuclear Weapons School
ATTN: Document Control

Director
Joint Strat. Tgt. Planning Staff JCS
ATTN: JPST, Capt G. D. Goetz
ATTN: JLTW-2

DEPARTMENT OF DEFENSE (Continued)

Chief
Livermore Division Fld. Command DNA
ATTN: FCPRL

Director
National Security Agency
ATTN: W14, Pat Clark
ATTN: Frank Leonard
ATTN: John Skillman, R52

OJCS/J-3
The Pentagon
ATTN: WWMCCS, Eval OFC, Mr. Toma

Under Sec'y of Def. for Rsch. & Engrg.
ATTN: S&SS (OS)

DEPARTMENT OF ARMY

Commander/Director
Atmospheric Sciences Laboratory
U.S. Army Electronics Command
ATTN: DELAS-AE-M, F. E. Niles

Director
BMD Advanced Tech. Ctr.
ATTN: ATC, W. Davies
ATTN: ATC-R, Don Russ
ATTN: ATC-T, Melvin T. Capps

Program Manager
BMD Program Office
ATTN: DACS-BMT, John Shea

Chief C-E Services Division
U.S. Army Communications Cmd.
ATTN: CC-OPS-CE

Commander
Harry Diamond Laboratories
ATTN: DRXDO-NP, Cyrus Moazed
ATTN: Mildred H. Weiner, DRXDO-TI
ATTN: DELHP-NP, Francis N. Wimenitz
ATTN: DELHD-RB, Robert Williams

Director
TRASANA
ATTN: TCC, F. Payan, Jr.
ATTN: ATAA-TAC, LTC John Hesse
ATTN: ATAA-SA

Director
U.S. Army Ballistic Research Labs.
ATTN: Lawrence J. Puckett

Commander
U.S. Army Comm-Elec. Engrg. Instal. Agy
ATTN: EED-PED, Ward Nair
ATTN: EED-PED, George Lane

DEPARTMENT OF ARMY (Continued)

Commander
U.S. Army Electronics Command
ATTN: DRSEL-NL-RD, H. S. Bennet
ATTN: DRSEL-PL-ENV, Hans A. Bomke

Commander
U.S. Army Foreign Science & Tech. Ctr.
ATTN: R. Jones
ATTN: P. A. Crowley

Commander
U.S. Army Materiel Dev. & Readiness Cmd.
ATTN: DRCLDC, J. A. Bender

Commander
U.S. Army Missile Command
ATTN: DRSMI-YTT, W. G. Preussel, Jr.

Commander
U.S. Army Missile Intelligence Agency
ATTN: Jim Gamble

Commander
U.S. Army Nuclear Agency
ATTN: MONA-WE, J. Berberet

Commander
U.S. Army Satcom Agency
ATTN: Document Control

DEPARTMENT OF NAVY

Chief of Naval Operations
ATTN: Op 943, LCDR Huff
ATTN: Ronald E. Pitkin
ATTN: Alexander Brandt

Chief of Naval Research
ATTN: Code 418
ATTN: Code 461

Commander
Naval Electronic Systems Command
ATTN: PME 117-T, Satellite Comm. Project Off.
ATTN: NAVALEX 034, T. Barry Hughes
ATTN: PME 117

Commanding Officer
Naval Intelligence Support Ctr.
ATTN: Mr. Dubbin, STIC 12

Commander
Naval Ocean Systems Center
ATTN: Code 0230, C. Baggett
ATTN: Code 532, William F. Moler
3 cy ATTN: Code 2200
ATTN: R. Eastman

Director
Naval Research Laboratory
ATTN: Code 7701, Jack D. Brown
ATTN: Code 5400, HG Comm. Dir. Bruce Wald
ATTN: Code 7700, Timothy P. Coffey
ATTN: Code 5460, Electromag Prop. Br.
ATTN: Code 5461, Trans. Inon. Prop.
ATTN: Code 5430, Staellite Comm.
ATTN: Code 5465, Prop, Applications

DEPARTMENT OF NAVY (Continued)

Commander
Naval Space Surveillance System
ATTN: CAPT J. H. Burton

Naval Space System Activity
ATTN: A. B. Hazzard

Officer-In-Charge
Naval Surface Weapons Center
ATTN: Code WA501, Navy NUC. Prgms. Off.

Commander
Naval Surface Weapons Center
ATTN: R. F. Butler, DF-14

Director
Strategic Systems Project Office
ATTN: NSSP-2722, Fred Wimberly
ATTN: NSP-2141

DEPARTMENT OF THE AIR FORCE

Commander
ADC/DC
ATTN: DC, Mr. Long

Commander
ADCOM/XPD
ATTN: XPQDQ

AF Geophysics Laboratory, AFSC
ATTN: PHD, John P. Mullen
ATTN: OPR, Alva T. Stair
ATTN: OPR, James C. Ulwick
ATTN: LKB, Kenneth S. W. Champion
ATTN: PHD, Jurgen Buchau
ATTN: OPR, Harold Gardner
ATTN: SUOL, Rsch. Lib.
ATTN: PHP, Jules Aarons

AF Weapons Laboratory, AFSC
ATTN: SUL
ATTN: CA, Arthur H. Guenther
ATTN: SAS, John M. Kamm
ATTN: DYC, Capt L. Wittwer

AFTAC
ATTN: TF, Maj Wiley
ATTN: TN

Air Force Avionics Laboratory, AFSC
ATTN: AAD, Wade Hunt
ATTN: AAB, H. M. Hartman
ATTN: AAD, Allen Johnson

Headquerters
Electronic Systems Division/XR
ATTN: XRE, Lt Michaels
ATTN: XRC, Lt Col J. Morin

Headquarters
Electronic Systems Division/YS
ATTN: YSEV

Headquarters
Electronic Systems Division, (AFSC)
ATTN: Jim Deas

DEPARTMENT OF THE AIR FORCE (Continued)

Commander
Foreign Technology Division, AFSC
ATTN: NICD, Library
ATTN: ETD, B. L. Ballard

HQ USAF/RD
ATTN: RDQ

Commander
Rome Air Development Center, AFSC
ATTN: V. Coyne, OCSE
ATTN: EMTLD, Doc. Library

Commander
Rome Air Development Center, AFSC
ATTN: ETEI, A. Lorentzen

SAMSO/MN
ATTN: MNNL, Lt Col Kennedy

SAMSO/SK
ATTN: SKA, Lt Maria A. Clavin

SAMSO/SZ
ATTN: SZJ, Maj Lawrence Doan

SAMSO/YA
ATTN: YAT, Capt L. Blackwelder

Commander-In-Chief
Strategic Air Command
ATTN: NRT
ATTN: ADWATE, Capt Bruce Bauer
ATTN: XPFS, Maj Brian G. Stephan

DEPARTMENT OF ENERGY

EG&G, Inc.
Los Alamos Division
ATTN: James R. Breedlove

University of California
Lawrence Livermore Laboratory
ATTN: Ronald L. Ott, L-531
ATTN: Tech. Info. Dept., L-3
ATTN: Donald R. Dunn, L-156
ATTN: Ralph S. Hager, L-31

Los Alamos Scientific Laboratory
ATTN: Doc. Con. for John Zinn
ATTN: Doc. Con. for R. F. Taschek
ATTN: Doc. Con. for John S. Malik
ATTN: Doc. Con. for Eric Jones

Sandia Laboratories
ATTN: Doc. Con. for D. A. Dahlgren, Org. 1722
ATTN: Doc. Con. for J. P. Martin, Org. 1732
ATTN: Doc. Con. for T. Wright
ATTN: Doc. Con. for A. Dean Thornbrough, Org. 1245
ATTN: Doc. Con. for W. D. Brown, Org. 1353

OTHER GOVERNMENT AGENCIES

Department of Commerce
Office of Telecommunications
ATTN: L. A. Berry
ATTN: G. Reed
ATTN: William F. Utlaut

OTHER GOVERNMENT AGENCIES (Continued)

NASA
Goddard Space Flight Center
ATTN: ATS-6, OFC P. Corrigan

National Oceanic & Atmospheric Admin.
Environmental Research Laboratories
ATTN: Joseph H. Pope
ATTN: C. L. Rufenach
ATTN: Richard Grubb

DEPARTMENT OF DEFENSE CONTRACTORS

Aerospace Corporation
ATTN: S. P. Bower
ATTN: T. M. Salmi
ATTN: Norman D. Stockwell
ATTN: SMFA for PWW
ATTN: F. A. Morse, A6 Rm. 2407
ATTN: V. Josephson
ATTN: J. E. Carter, 120, Rm. 2209
ATTN: Irving M. Garfunkel
ATTN: F. E. Bond, A1, Rm. 5003
ATTN: D. P. Olsen, 120, Rm. 2224E

Analytical Systems Engineering Corp.
ATTN: Radio Sciences

The Boeing Company
ATTN: D. Murray
ATTN: Glen Keister

Brown Engineering Company, Inc.
Cummings Research Park
ATTN: Romeo A. Deliberis

University of California at San Diego
Marine Physical Lab. of the Scripps
Institute of Oceanography
ATTN: Henry G. Booker

Charles Stark Draper Laboratory, Inc.
ATTN: J. P. Gilmore, MS 63
ATTN: D. B. Cox

Computer Sciences Corporation
ATTN: H. Blank

Comsat Laboratories
ATTN: R. R. Taur

Cornell University
Department of Electrical Engineering
ATTN: D. T. Farley, Jr.

ESL, Inc.
ATTN: J. Roberts
ATTN: C. W. Prettie
ATTN: James Marshall
ATTN: V. L. Mower

Ford Aerospace & Communications Corp.
ATTN: J. T. Mattingley, MS X22

General Electric Company
Space Division
Valley Forge Space Center
ATTN: M. H. Bortner Space Sci. Lab.

General Electric Company
ATTN: F. A. Reibert

DEPARTMENT OF DEFENSE CONTRACTORS (Continued)

General Electric Company
TEMPO-Center for Advanced Studies
ATTN: Tim Stephens
ATTN: Tom Barrett
ATTN: B. Gambill
ATTN: William McNamera
ATTN: Warren S. Knapp
ATTN: Mack Stanton
ATTN: Don Chandler
ATTN: DASIAC

General Research Corporation
ATTN: Joel Garbarino
ATTN: John Ise, Jr.

Geophysical Institute
University of Alaska
ATTN: T. N. Davis
ATTN: Neal Brown
ATTN: Technical Library

GTE Sylvania, Inc.
Electronics Systems Grp.-Eastern Div.
ATTN: Marshal Cross

HSS, Inc.
ATTN: Donald Hansen

University of Illinois
Department of Electrical Engineering
ATTN: K. C. Yeh

Institute for Defense Analyses
ATTN: Ernest Bauer
ATTN: Joel Bengston
ATTN: Hans Wolfhard
ATTN: J. M. Aein

Intl. Tel. & Telegraph Corporation
ATTN: Technical Library

JAYCOR
ATTN: S. R. Goldman

Johns Hopkins University
Applied Physics Laboratory
ATTN: Document Librarian
ATTN: Thomas Potemra
ATTN: John Dassoulas

Kaman Sciences Corporation
ATTN: B. J. Bittner

Linkabit Corporation
ATTN: Irwin Jacobs

Lockheed Missiles & Space Co., Inc.
ATTN: D. R. Churchill
ATTN: Dept. 60-12

Lockheed Missiles and Space Co., Inc.
ATTN: Richard G. Johnson, Dept. 52-12
ATTN: Martin Walt, Dept. 52-10

M.I.T. Lincoln Laboratory
ATTN: Mr. Walden, X113
ATTN: James H. Pannell, L-246
ATTN: Lib. A-082 for David M Towle
ATTN: D. Clark

DEPARTMENT OF DEFENSE CONTRACTORS (Continued)

McDonnell Douglas Corporation
ATTN: J. Moule
ATTN: George Mroz
ATTN: William Olson
ATTN: N. Harris

Mission Research Corporation
ATTN: Steven L. Gutsche
ATTN: Ralph Kilb
ATTN: R. Hendrick, Jr.
ATTN: R. Bogusch
ATTN: Dave Sowle
ATTN: P. Fischer
ATTN: F. Fajen
ATTN: M. Scheibe
ATTN: Warren A. Schlueter
ATTN: W. F. Crevier
ATTN: D. Sappenfield
ATTN: Conrad L. Longmire
5 cy ATTN: Tech. Lib.

The Mitre Corporation
ATTN: C. E. Callahan
ATTN: Chief Scientist, W. Sen
ATTN: G. Harding

Pacific-Sierra Research Corp.
ATTN: E. C. Field, Jr.

Photometrics, Inc.
ATTN: Irving L. Kofsky

Physical Dynamics, Inc.
ATTN: E. J. Fremouw

Physical Dynamics Inc.
ATTN: Joseph B. Workman
ATTN: A. Thompson

R & D Associates
ATTN: William J. Karzas
ATTN: Robert E. Lelevier
ATTN: William B. Wright, Jr.
ATTN: Forrest Gilmore
ATTN: Bryan Gabbard

The Rand Corporation
ATTN: Ed Bedrozian
ATTN: Cullen Crain

Raytheon Company
ATTN: Barbara Adams

Science Applications, Inc.
ATTN: E. A. Straker
ATTN: Daniel A. Hamlin
ATTN: Curtis A. Smith
ATTN: D. Sachs
ATTN: Lewis M. Linson
ATTN: Jack McDougall

Science Applications, Inc.
Hunstville Division
ATTN: Dale H. Divis

System Development Corporation
ATTN: E. G. Meyer

DEPARTMENT OF DEFENSE CONTRACTORS (Continued)

SRI International
ATTN: Alan Burns
ATTN: Walter G. Chesnut
ATTN: Charles L. Rino
ATTN: Ray L. Leadabrand
ATTN: Walter Jaye
ATTN: M. Baron
ATTN: G. Smith
ATTN: L. L. Cobb
ATTN: Donald Neilson
ATTN: David A. Johnson

DEPARTMENT OF DEFENSE CONTRACTORS (Continued)

Technology International Corporation
ATTN: W. P. Boquist

Tri-Com, Inc.
ATTN: Darrel Murray

TRW Defense & Space Sys. Group
ATTN: R. K. Plebuch, R1-2078

Visidyne, Inc.
ATTN: Charles Humphrey
ATTN: J. W. Carpenter